HHS Public Access

Author manuscript

Cell. Author manuscript; available in PMC 2023 January 20.

Published in final edited form as:

Cell. 2022 January 20; 185(2): 311–327.e24. doi:10.1016/j.cell.2021.12.022.

Vision-dependent specification of cell types and function in the developing cortex

Sarah Cheng[1,2,6], **Salwan Butrus**[3,6], **Liming Tan**[1,6], **Runzhe Xu**[1], **Srikant Sagireddy**[3], **Joshua T. Trachtenberg**[4], **Karthik Shekhar**[3,5,*], **S. Lawrence Zipursky**[1,*,#]

[1]Department of Biological Chemistry, Howard Hughes Medical Institute, David Geffen School of Medicine, University of California, Los Angeles, Los Angeles, CA 90095, USA

[2]Department of Ophthalmology, Stein Eye Institute, David Geffen School of Medicine, University of California, Los Angeles, Los Angeles, CA, 90095, USA.

[3]Department of Chemical and Biomolecular Engineering; Helen Wills Neuroscience Institute; California Institute for Quantitative Biosciences, QB3, University of California, Berkeley, CA, USA 94720

[4]Department of Neurobiology, David Geffen School of Medicine at UCLA, Los Angeles, CA 90095, USA

[5]Faculty Scientist, Biological Systems and Engineering Division, Lawrence Berkeley National Laboratory, CA, USA 94720

[6]These authors contributed equally

SUMMARY

The role of postnatal experience in sculpting cortical circuitry, while long appreciated, is poorly understood at the level of cell types. We explore this in the mouse primary visual cortex (V1) using single-nucleus RNA-sequencing, visual deprivation, genetics, and functional imaging. We find that vision selectively drives the specification of glutamatergic cell types in upper layers (L) (L2/3/4), while deeper-layer glutamatergic, GABAergic, and non-neuronal cell types are established prior to eye opening. L2/3 cell types form an experience-dependent spatial continuum defined by the graded expression of ~200 genes, including regulators of cell adhesion and synapse formation. One of these, *Igsf9b*, a vision-dependent gene encoding an inhibitory synaptic cell

[*]Correspondence: Karthik Shekhar (kshekhar@berkeley.edu), S. Lawrence Zipursky (lzipursky@mednet.ucla.edu).
[#]Lead contact

AUTHOR CONTRIBUTIONS

S.C., L.T., J.T.T., and S.L.Z conceived the project. S.C., L.T. and S.L.Z. designed snRNA-seq experiments. S.B. and K.S. conceived and designed the computational methods for transcriptomic analysis. S.C. carried out snRNA-seq and initial bioinformatic analysis. S.B. and S.S. performed the transcriptomic analysis. S.C. and V.X designed and carried out FISH experiments and characterized expression of synaptic markers. L.T. carried out live imaging of circuit activity in wild type and mutant mice. S.C, S.B., L.T., J.T.T., K.S., and S.L.Z analyzed the data. S.C., S.B., K.S. and S.L.Z. wrote the paper with input from L.T. and J.T.T.

DECLARATION OF INTERESTS

The authors declare no competing interests

adhesion molecule, is required for the normal development of binocular responses in L2/3. In summary, vision preferentially regulates the development of upper-layer glutamatergic cell types through the regulation of cell type-specific gene expression programs.

Graphical Abstract

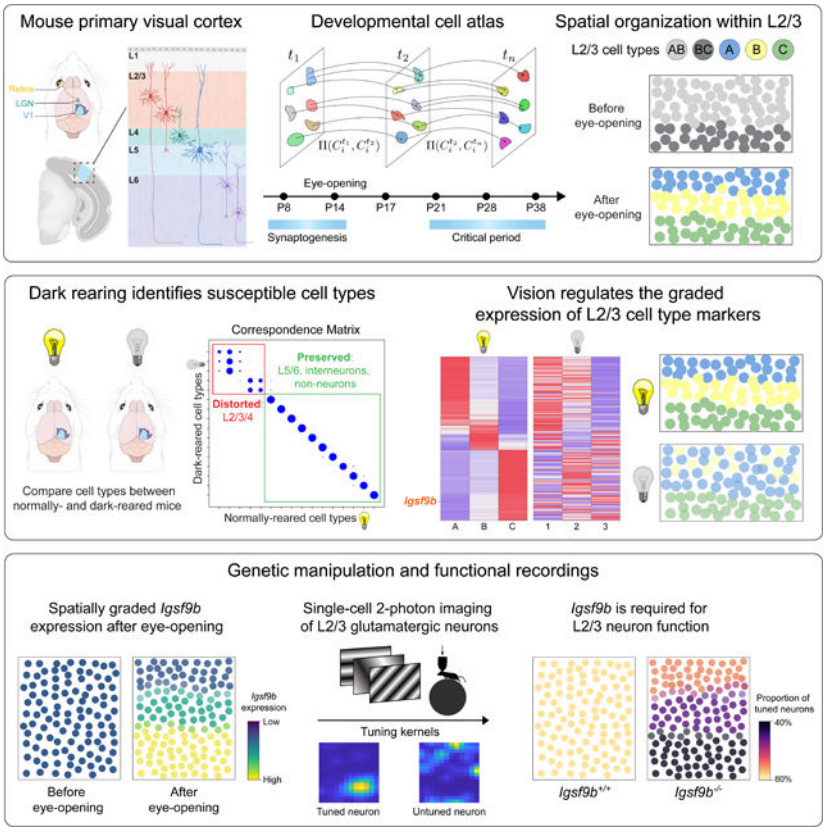

In brief

Transcriptomic, genetic, and functional analysis of the developing mouse primary visual cortex (V1) reveals that early sensory experience selectively influences the development of layer 2/3 glutamatergic neurons by regulating spatial and temporal gene expression programs.

INTRODUCTION

The establishment of neural circuitry in the mammalian cortex relies on the interaction of the developing postnatal animal with its environment. Cortical circuits comprise diverse cell types interconnected by complex synaptic networks (Motta et al., 2019; Tasic et al., 2016). The formation of this circuitry relies on genetically hard-wired mechanisms mediated by cell recognition molecules and sensory-independent neural activity (Ackman et al., 2012; Katz and Shatz, 1996; Ko et al., 2013; Meister et al., 1991; Sanes and Zipursky, 2020; Xu et al., 2011). During postnatal development, experience-dependent processes are required for the maturation of this circuitry (Hensch, 2004, 2005; Hooks and Chen, 2020; Ko et al., 2013; Wiesel and Hubel, 1963). These periods of developmental plasticity, known as “critical

periods", are observed in sensory cortical areas and regulate processes such as language development and cognition (Reh et al., 2020).

The influence of experience on cortical circuitry in the primary visual cortex (V1) is accessible to molecular, genetic, and functional analysis in the mouse and thus is well suited for mechanistic studies (Hooks and Chen, 2020). Neural circuitry is patterned by vision (Gordon and Stryker, 1996; Tan et al., 2020) and this process can be studied through longitudinal calcium imaging of neurons in V1 of awake behaving animals (Tan et al., 2021; Tan et al., 2020). Mice open their eyes around postnatal day (P)14. Binocular circuitry is sensitive to vision after eye opening, but its peak period of sensitivity, demonstrated and defined by the effects of monocular deprivation on cortical ocular dominance, begins about a week after eye opening (~P21) and continues through ~P35 (Espinosa and Stryker, 2012; Gordon and Stryker, 1996). Visual experience during this period is necessary for the development and maintenance of the neural circuitry underlying binocular vision (Espinosa and Stryker, 2012; Gordon and Stryker, 1996; Ko et al., 2013; Ko et al., 2014; Tan et al., 2021; Tan et al., 2020; Wang et al., 2010).

Recent advances in single-cell transcriptomics have uncovered a vast neuronal diversity in the adult mouse V1 (Hrvatin et al., 2018; Tasic et al., 2016; Tasic et al., 2018). Previous investigations of vision-dependent changes in gene expression during the critical period have relied on comparing bulk transcriptomic profiles of V1 between normally reared and visually deprived animals (Majdan and Shatz, 2006; Mardinly et al., 2016; Tropea et al., 2006), or within normally reared animals at different points during the critical period (Lyckman et al., 2008). Consequently, these studies did not investigate vision-dependent gene expression at the level of the diverse cell types in V1. This resolution is crucial to understanding the mechanisms by which experience regulates neural circuitry at the molecular, cellular, and functional levels.

Here, we studied the role of vision in the development of V1 cell types and their circuitry in mice by combining single-nucleus transcriptomics, statistical inference, sensory perturbations, genetics, and *in vivo* functional imaging. We assembled a developmental transcriptomic atlas of postnatal mouse V1. Using this as a foundation, we discovered that: 1) Vision is required for the establishment and maintentance of L2/3 glutamatergic types, but not other cell types in V1; 2) L2/3 glutamatergic cell types are organized as sublayers in V1 and form a transcriptomic continuum through the graded expression of ~200 genes; and 3) Among these genes, *Igsf9b*, a vision-regulated cell adhesion molecule, is required in a graded fashion for the functional maturation of L2/3 glutamatergic neurons. Together, our study establishes a framework for future investigations of how experience regulates cell type specification in the brain.

RESULTS

Transcriptional profiling of mouse V1 development using single-nucleus RNA-seq

To survey the transcriptomic diversity and maturation of cells in V1, we used droplet-based single-nucleus (sn) RNA-seq to profile this region during postnatal development in normally reared mice (Figures 1A and S1D). We collected samples from six postnatal time points:

P8, P14, P17, P21, P28 and P38 (Figure 1B). Three of these are prior to the classical critical period for ocular dominance plasticity, with synaptogenesis occurring between P8 and eye-opening (P14) (Hinojosa et al., 2018; Li et al., 2010) (Figures S1A–C), and the remaining three span the critical period of ocular dominance plasticity (Gordon and Stryker, 1996; Tan et al., 2020; Wang et al., 2010), including its start (P21), peak (P28), and closure (P38).

Data from each timepoint consisted of four single-nuclei library replicates, each derived from cells collected from multiple mice (STAR Methods). The resulting gene expression matrices were filtered to remove low-quality cells and doublets (Wolock et al., 2019), as well as cells with a high proportion of mitochondrial transcripts (>1%). In total, we obtained 144,725 high-quality nuclear transcriptomes across the six time points (Figures S1D–H).

A postnatal developmental atlas of V1 cell classes, subclasses, and types

We used dimensionality reduction and clustering to derive a developmental taxonomy consisting of cell classes, subclasses, and types (Yao et al., 2021a; Yao et al., 2020; Yuste et al., 2020; Zeng and Sanes, 2017) at each of the six time points (Figures 1C, D and S1D; STAR Methods). Cell classes consisted of glutamatergic neurons (n=92,856; 3176 genes/cell detected on average), GABAergic neurons (n=13,374; 2966 genes/cell), and non-neuronal cells (n=38,495; 1549 genes/cell) identified by canonical markers (Figure S1I and Table S1) (Hrvatin et al., 2018; Tasic et al., 2016; Tasic et al., 2018). The relative proportions of the three cell classes were consistent across biological replicates (data not shown).

Glutamatergic cells separated into eight subclasses within the four cortical layers - L2/3, L4, L5IT, L5NP, L5PT, L6CT, L6IT, and L6b (Figures 2A, B). We also identified six GABAergic subclasses, which included the four well-known groups defined by the selective expression of *Pvalb*, *Sst*, *Vip*, and *Lamp5* (Zeng and Sanes, 2017) and two smaller subclasses that selectively expressed the genes *Stac* and *Frem1*. Non-neuronal cells included oligodendrocytes, oligodendrocyte precursor cells, astrocytes, vascular and leptomeningeal cells, endothelial cells, and microglia (Figure 1D). Similar results were obtained using an alternative computational pipeline (Satija et al., 2015) (Figure S1K). We found a tight correspondence between the transcriptome-wide gene signatures that defined developing subclasses in our dataset and the subclasses identified in a recent survey of the adult mouse cortex (Tasic et al., 2018) (Figure S1J).

The relative proportions of most neuronal subclasses were stable over time (Figures 2C and S1L), although proportions of non-neuronal subclasses varied (Figure S1M). This suggests that the neuronal subclass composition of V1 is established before P8, our earliest time point. We also identified subclass-specific markers (Figures 2B, S2A–E, and Table S3). This included *Ccbe1* (collagen and calcium-binding EGF domain-containing protein 1), which is specific for L2/3 glutamatergic neurons throughout development (Figures 2D and S2A–C).

Next, we performed dimensionality reduction and clustering for each class at each age separately. We henceforth refer to transcriptomically distinct clusters as types. The eight glutamatergic subclasses separated into 14–16 types, the six GABAergic subclasses separated into 14–15 types, and the six non-neuronal subclasses separated into 9–11 types

depending upon age (Figure 1D) (STAR Methods). Post-hoc differential expression analysis identified robust cell type-specific markers at each age (Figures S3A–C, Table S4).

Transcriptomic identities of L2/3 and 4 neuron types are established after eye opening

While the number of cell types within each class was similar at each age, it was not immediately clear how types identified at different ages were related to each other. Using transcriptomic similarity as a proxy for temporal relationships, we tracked the postnatal maturation of types within each class using a supervised classification framework (STAR Methods). We observed striking subclass-specific differences in the maturation of glutamatergic neuron types (Figure 2E). L5, and to a slightly lesser extent L6, neuron types tightly corresponded throughout the time course, indicating that these types are established prior to eye-opening, and maintained. Conversely, upper-layer neuron types (L2/3 and L4) exhibited poor correspondences, suggesting gradual specification. Within L2/3, two neuron types at P8 and P14 matured into three types after eye-opening. By contrast, differences in the maturational patterns of GABAergic and non-neuronal subclasses were less pronounced (Figures S2F–I, STAR Methods).

These subclass-specific differences in the timing of glutamatergic neuron type development are supported by five quantitative observations: 1) L5/6 types at different ages could be related in a 1:1 fashion with each other while L2/3/4 types could not be. These differences were based on the Adjusted Rand index (ARI), a measure of transcriptomic correspondence between two sets of clusters (Figure 2F). Furthermore, the clustering results for L2/3 and L4 were more sensitive ($P<0.0001$, one-way ANOVA) to changes in the resolution parameter than for L5 and L6 (Figure 2G); 2) The transcriptomic separation among L2/3 and L4 types was lower than that among L5 and L6 types, GABAergic types, and non-neuronal types at all ages (Figures S2J–L); 3) Differentially expressed genes that distinguished L2/3 and L4 neuron types varied with age, whereas those that defined L5 and L6 neuron types were stable (Figures S3D–G); 4) In a statistical test to identify temporally differentially expressed (tDE) genes in each layer (see STAR Methods), L2/3 and 4 contained twice as many tDE genes as L5 and 6 (Figure S3H); and 5) The relative frequency of L2/3 and L4 types varied over time (see below). By contrast, the relative proportions of the ten L5 and L6 types, the smallest of which was present at an overall frequency of 1%, were stable throughout the time course. Together, these results suggest that within glutamatergic neurons of V1, transcriptomic specification of types within upper-layer subclasses (L2/3 and L4) occurs later than types in lower-layer subclasses (L5 and L6).

L2/3 neuron types are spatially segregated

We classified L2/3 glutamatergic neurons into three types (A, B, and C) beginning at P17, the first time point assessed after the onset of vision at P14 (Figure 3A). These were visualized in tissue using *in situ* hybridization for marker genes *Cdh13*, *Trpc6*, and *Chrm2* for types L2/3_A, L2/3_B, and L2/3_C, respectively (Figures 3B–D). Within the L2/3 glutamatergic neuron subclass, these transcripts are specific for the aforementioned glutamatergic types. They are, however, expressed in other subclasses as well. Cells expressing the three transcripts were organized into sublayers that became more pronounced with age: L2/3_A close to the pia, L2/3_C bordering L4, and L2/3_B in between (Figures

3D, E). At the boundaries of these sublayers, cells co-expressed more than one type-specific marker, indicating a lack of discrete, sharp boundaries, and mirroring the continuous transcriptomic arrangement observed *in silico* (see below).

Prior to the onset of vision (P8 and P14), however, only two transcriptomic types were resolved. We denote these AB and BC. AB and BC were organized as two sublayers based on their differential expression of *Cdh13* and *Chrm2* (Figures 3C and S4A–E), with cells at the border co-expressing the two markers. In contrast, the B marker *Trpc6* was weakly expressed in cells scattered throughout L2/3 at these early stages (Figures 3B–C, E–H, and S4D, E). There is a striking difference in the distribution of *Cdh13* between P8 and P38. At P8, *Cdh13* extends to deep sublayers of L2/3, whereas by P38, expression is restricted to a narrow strip of cells at the top of L2/3. By contrast, *Chrm2* expression extends slightly more towards upper sublayers at P38. Multiple A-, B-, and C-specific markers were not expressed before P14 and only appeared at later stages (Figure S3D). Thus, we infer that the L2/3 glutamatergic types A, B, and C arise from AB and BC types following the onset of vision (Figure 2E and STAR Methods).

Vision is necessary for establishing and maintaining L2/3 neuron type identity

The emergence of three L2/3 neuron types following eye-opening prompted us to explore the role of vision in defining cell types. It is well established that vision is required for the development of cortical circuitry during the critical period for ocular dominance plasticity (P21-P38) (Espinosa and Stryker, 2012; Gordon and Stryker, 1996). We used snRNA-seq to profile V1 in animals that were dark-reared from P21 to P28 and P21 to P38. For brevity, these experiments are referred to as P28DR and P38DR, respectively (DR = dark rearing). We also profiled animals that were exposed to 8 hours of ambient light after dark-rearing from P21-P28 to assess the impact of visual stimulation following prolonged deprivation (Figure 4A). We refer to this experiment as P28DL (DL = dark-light). In total, we recovered 77,150 high-quality nuclei across these three experiments and identified classes, subclasses, and types using the same computational pipeline applied to the normally reared (NR) samples (Figure 4B and STAR Methods).

We performed three computational analyses to probe the effect of visual deprivation (DR and DL) on the transcriptomic patterns observed in normally reared (NR) mice. First, we compared the overall transcriptional profiles of cell types across the three conditions. We found that dark rearing disrupted the type identities of L2/3 and L4, but not L5 and L6, glutamatergic neurons (Figures 4C and S5F). Furthermore, dark rearing neither altered the gene expression patterns that defined subclasses nor those defining GABAergic and non-neuronal cell types (Figures S5A–C). Second, the cell type markers identified in NR mice were disrupted by dark rearing in L2/3, and slightly in L4, but not L5 and 6 (Figures 4D–E and S5D–E). Third, we probed the effect of visual deprivation on type-specific genes within each layer. While the signatures within all four layers were different when comparing DR to NR, the effect was most dramatic for L2/3 (Figure S6H). Thus, vision selectively influences transcriptomic profiles of upper-layer glutamatergic cell types.

The effect of dark rearing was particularly striking in L2/3. The L2/3 clusters observed in dark-reared mice poorly resembled the three types in normally reared animals, and the

expression patterns of cell type-specific marker genes were disrupted (Figure 4C, D). By contrast to the three sublayers highlighted by *Cdh13, Trpc6,* and *Chrm2* expression in L2/3 in normally reared mice, only two sublayers were observed in dark-reared mice. Notably, there was a sharp decrease in *Trpc6*-expressing cells (Figure 4F–J), consistent with snRNA-seq data (Figure 4D). There was also an increase in the number of *Cdh13*-expressing cells and the domain of expression extended into deeper layers. This was not simply a loss of one cell type, however, but a global disruption of gene expression patterns throughout L2/3 (see below, Figure 6). The two-layered pattern was more prominent in dark-reared animals at P38 compared to P28 (Figures 4G–I and S5H–I). Thus, in the absence of vision, the expression patterns of these markers were similar to those prior to the onset of vision (see panels P8 and P14 in Figure 3E).

The loss of cell type identity in animals deprived of light during the first half of the critical period was partially reversible. L2/3 transcriptomic clusters in mice exposed to 8 hours of ambient light after dark rearing between P21-P28 showed a marked recovery of gene expression patterns observed in normally reared animals (Figures 4C–D and S5G, S6H). In addition, the layered arrangement of *Cdh13*-, *Trpc6*- and *Chrm2*-expressing cells in these animals was also shifted towards that observed in normally reared animals (Figures 4F–J and S5H–I). These results demonstrate that vision is needed to maintain the transcriptomic and spatial identities of L2/3 cell types.

As the spatial expression of cell type markers in the absence of vision and at eye opening were similar, we set out to assess whether vision was not only necessary to maintain cell types, but also required for their establishment. To test this, we dark-reared mice from P8 to P17 (Figure 5A) and assessed the expression patterns of *Cdh13*, *Trpc6*, and *Chrm2* in tissue sections. These mice had two, instead of three, sublayers within L2/3, similar to P8 and P14 normally reared animals (Figures 5B–D). These changes included a dramatic reduction in *Trpc6*-expressing cells and an increase in *Cdh13* expression, which was accompanied by an expansion in its expression domain towards the middle sublayer in mice with no visual experience (Figure 5E). This was not a general effect on glutamatergic cell types, as the relative proportions of L5 neuron types were insensitive to changes in visual experience (Figure S4G–H). In summary, these results show that vision acts selectively in L2/3 to establish and maintain cell types.

Continuous variation of L2/3 neuron types and gene expression gradients are shaped by vision

The sublayers corresponding to types A, B, and C in L2/3 were partially overlapping, mirroring the continuous arrangement of their transcriptomes (see Figures 3A, E). Consistent with this continuous arrangement, more than 70% of the 285 differentially expressed genes among the L2/3 types in normally reared mice exhibited graded, rather than digital, differences (Figures 6A and S6A–H). In dark-reared mice, these genes were no longer expressed in a graded fashion between the L2/3 clusters, although their overall (i.e., bulk) expression levels, for all but a few genes, were unaltered (Figures S6C). These gradients were partially recovered by brief restoration of normal visual experience to dark reared animals during the critical period (Figure 6A). Thus, vision selectively regulates gene

expression in a sublayer-specific fashion, contributing to the continuous variation of L2/3 cell types.

We hypothesized that graded genes which are temporally regulated and expressed in a vision-dependent manner could be associated with functional changes in L2/3 during the critical period. Several genes fit this description, including cell surface molecules (CSMs) and transcription factors (TFs) (Figures 6B, C and S6I, J). Among these were cell surface and secreted proteins previously shown to be involved in the development of neural circuits, including proteins regulating cell recognition (e.g., *Kirrel3*, *Sdk2*) and synaptic adhesion (e.g., *Tenm1* and *Cbln2*) (Figures 6B, C).

To identify candidate cell surface proteins from this set that may contribute to vision-dependent changes in circuitry during the critical period, we selected genes that satisfied three criteria across all L2/3 glutamatergic types: 1) Selective upregulation during the critical period; 2) Downregulation in DR animals; and 3) Upregulation in DR animals in response to eight hours of ambient light at P28 (i.e., P28DL mice). Five genes (*Igsf9b*, *Epha10, Cdh4*, *Sdk2*, and *Sema4a*) satisfied all three criteria (Figures 6E–F) and all five encode cell surface proteins implicated in regulating neuronal wiring, raising the possibility that they contribute to experience-dependent circuit development in L2/3. As the expression levels and dynamics of *Igsf9b* were the most robust of this group, we explored its function during the critical period.

Igsf9b knock-out alters inhibitory synapses in L2/3

IGSF9B is a homophilic cell adhesion molecule of the immunoglobulin superfamily that promotes Neuroligin2 (Nlgn2)-dependent inhibitory synapse formation (Lu et al., 2017; Woo et al., 2013) (Figure 6D). This protein is of particular interest because inhibition plays an important role in regulating V1 circuitry during the critical period (Reh et al., 2020). We assessed the spatial distribution of *Igsf9b* transcripts in L2/3 at different times in development using FISH (Figure 6G) and *in silico* by regarding the transcriptomic positions of L2/3 neurons in gene expression space as “pseudo” spatial coordinates (Figure 6H; STAR Methods). *Igsf9b* levels were low prior to eye opening and increased during the critical period in a graded manner favoring increased expression deeper into L2/3. Sensory activity further modulated the expression level and lamination of *Igsf9b*. Dark-rearing during the critical period decreased *Igsf9b* expression and slightly disrupted its graded expression in L2/3 neurons (Figures 6F, I, J and Figure S6K). These effects were reversed and *Igsf9b* expression levels were upregulated when dark-reared animals were exposed to ambient light for 8 hrs. Given the graded expression of *Igsf9b* across sublaminae increasing from upper to lower layers, it was particularly intriguing that a second gene encoding another Ig superfamily protein, Mdga1, a negative regulator of Nlgn2 (Figure 6D), was expressed in a graded and opposite spatial pattern to *Igsf9b* (Figure 6G, H; Figure S6F). Together, the spatiotemporal dynamics of *Igsf9b* and *Mdga1* expression after eye opening form a gradient of inhibitory synapse potential along the pial-ventricular axis of L2/3, with lower sublayers exhibiting increased inhibition.

To explore the role of *Igsf9b* in the development of inhibitory synapses in L2/3, we examined the expression of five markers of inhibitory synapses in wild-type (WT) and

Igsf9b knock-out (KO) mice. These markers included three postsynaptic proteins (Gamma-aminobutyric acid Type A receptor subunit alpha 1 (GABRA1), Neurolign2 (NLGN2), and Gephryin (GPHN)) and two presynaptic proteins (the presynaptic vesicular GABA transporter (VGAT) and the enzyme glutamic acid decarboxylase (GAD65)) (Figure S7A). Expression levels of the postsynaptic markers GABRA1 and NGLN2 were significantly decreased in P37 KO mice relative to WT littermates (Figure S7B), although GPHN remained unchanged (not shown). By contrast, there was an increase in the levels of presynaptic markers GAD65 and VGAT (Figure S7B); this increase may reflect a homeostatic response to the changes reflected in the decrease in postsynaptic markers. Consistent with our finding that expression of *Igsf9b* in L2/3 increases with depth, these phenotypes were more pronounced toward the bottom of L2/3 (Figure S7D–G; see Figure 6G, H). By contrast, excitatory synapse markers were unaffected in KO mice (Figure S7C). Thus, loss of *Igsf9b* specifically affects inhibitory synapses in a graded fashion along the L2/3 pial-ventricular axis.

Igsf9b regulates vision-dependent maturation of binocular circuitry

A defining feature of the critical period in V1 is the vision-dependent maturation of binocular neurons, which are required for depth perception, also known as stereopsis (La Chioma et al., 2019). To mediate stereopsis, these neurons must selectively respond to the same kind of visual information from both eyes (binocular matching). Although binocular neurons can be detected shortly after eye opening, they exhibit poor matching at early stages. Visual experience during the critical period (P21-P36) changes the population of binocular cells; binocular cells that are poorly tuned are rendered monocular and new well-tuned binocular neurons arise from well-tuned monocular neurons through recruitment of matched inputs from the other eye (Tan et al., 2021; Tan et al., 2020).

We examined whether *Igsf9b* is required for the normal development of binocular responses in L2/3 using *in vivo* 2-photon calcium imaging in binocular V1 (Figure S7H, I). This region of V1 comprises not only neurons responsive to both eyes (i.e., binocular cells), but also monocular neurons responsive to stimuli presented to the ipsilateral or contralateral eye only. We measured responses of thousands of excitatory neurons to stimulation of each eye at P21 and P36 in normally reared WT and *Igsf9b* KO mice (Figure 7A; see STAR Methods). These results were also compared to those from GCaMP6s transgenic mice that were normally reared (NR) or dark-reared (DR) during the critical period (Tan et al., 2020) (Figure 7A). Neuronal responses were measured at three depths, spanning the top (type A), middle (type B), and bottom (type C) sublayers of L2/3, corresponding to the regions of low, intermediate, and high *Igsf9b* expression, respectively (Figure 7B–D, Figure S7J–L; see STAR Methods). At P21, the proportion of binocular neurons and their orientation matching in KO mice were indistinguishable from those in WT (Figure 7E). This is consistent with the low expression of *Igsf9b* in L2/3 before P21 (Figure 7A, see Figure 6). At P36, after closure of the critical period—when *Igsf9b* expression would normally have increased—only about half the normal number of binocular neurons were observed in KO mice, and these few neurons displayed poor binocular matching (Figure 7F). This phenotype resembles that observed in DR mice (Figure 7G).

We also noted a marked decrease in the proportion of tuned cells in KO mice. Untuned cells were active, but by contrast to tuned cells, they were not responsive to specific visual stimuli in a time-locked fashion (Figure 7H, I). While visual deprivation decreased the proportion of visually responsive neurons from 75% (NR) to 66% (DR), *Igsf9b* KO decreased the proportion of responsive neurons to 47% by P36 (Figure 7J). This reduction in proportion of tuned neurons in KO mice from P21 to P36 correlated with a marked reduction in the signal to noise ratios (SNRs) of neuronal responses at critical period closure (Figure 7K, left and middle panels). The extent of SNR impairment in KO was more severe than in DR mice (Figure 7K, compare middle and right panels). Notably, the severity of reduction of tuned neurons in KO increased with depth (Figure 7L), mirroring the graded expression of *Igsf9b* in L2/3 types A, B, and C along the pial-ventricular axis in normally reared WT mice (see Figure 6). Taken together, these findings establish that *Igsf9b* regulates the vision-dependent maturation of L2/3 excitatory neurons in a graded fashion along L2/3 pial-ventricular axis.

DISCUSSION

Critical periods define windows of postnatal development where neural circuitry is particularly sensitive to experience. Here we sought to gain insight into how experience influences circuitry during this period at the level of cell types in mouse V1.

A postnatal developmental atlas of mouse V1

To study vision-dependent cortical development at the level of cell types, we generated a developmental atlas of mouse V1 comprising over 220,000 nuclear transcriptomes spanning six postnatal ages and three light-rearing conditions. Several features of this dataset enabled us to identify robust and reproducible biological signals. First, we identified a similar number of transcriptomic clusters at all six ages, which were collected and processed separately. For all clusters, transcriptomic identities and relative proportions were comparable between independent samples, consistent with these being bona fide cell types. Second, computational inference of transcriptomic maturation showed that the GABAergic, deep-layer glutamatergic, and non-neuronal cell types were present prior to eye opening and remained largely unchanged through the critical period, whether animals were reared in a normal dark/light cycle or in the dark. Third, these stable cell types served as important “negative controls” that enabled us to identify the minority of cell types among the upper layer glutamatergic neurons that were specified following eye opening, and whose transcriptomic identities were profoundly influenced by vision. Fourth, we identified cell type markers that enabled us to uncover the arrangement of L2/3 cell types in sublayers (see Figures 3B–D). And finally, the developmental atlas served as a foundation to investigate vision-dependent functional maturation of V1 at the resolution of cell types and molecules.

The establishment and maintenance of L2/3 neuron types require vision

In this study, we define a cell type based on a core transcriptomic signature that distinguishes it from other types. When the signature becomes invariant during development, we consider the cell type to be specified. For L2/3 and 4 cell types, these signatures are established following eye-opening, whereas for the remaining cell types, they are present from P8. These signatures allow us to assess cell type-specific gene regulation under sensory

deprivation. While activity-dependent gene expression changes occur in every layer, the changes are more extensive in L2/3 and 4, where cell type identity is disrupted. This is not the case for deeper layers (L5 and 6).

It is striking that the acquisition of transcriptomic cell type identity in L2/3 excitatory neurons follows a time course similar to their functional maturation. We previously showed that there are few binocular neurons in L2/3 at eye opening. Their numbers increase over the next several days in a vision-dependent process (Tan et al., 2021). During the critical period, these binocular neurons, most of which are poorly tuned, are rendered monocular. In parallel, new binocular neurons are formed from the conversion of other well-tuned monocular neurons which gained matched responses to the other eye (Tan et al., 2020). It is through this exchange of neurons that well-tuned and matched binocular neurons emerge to give rise to mature binocular circuitry. This process relies on vision during the critical period. Activity may drive cell type changes that, in turn, instruct changes in circuit organization, or alternatively, transcriptomic programs could be regulated by circuit activity. Further experiments will be necessary to distinguish between these and other mechanisms. Experience-dependent regulation of upper-layer cortical cell types may be a general principle underlying cortical development during critical periods.

Continuous variation in L2/3 identity and sublayer arrangement

Although unsupervised clustering defined three predominant glutamatergic neuronal types in L2/3, the gene expression differences between them were graded, giving rise to continuous variation in transcriptomic identity (Figures 6A and S6A–B). This continuous variation *in silico* was seen as a spatially graded, sublayered arrangement in L2/3 via FISH. This is not a general feature of glutamatergic cell type specification, as glutamatergic cell type identity in L5, for example, is neither graded nor dependent upon vision. Continuous variation of cell type identity has been reported in other regions of the mammalian brain (Cembrowski et al., 2016; Cembrowski and Menon, 2018; O'Leary et al., 2020; Yao et al., 2021b).

That the molecular heterogeneity in L2/3 reflects functional differences is supported by a recent retrograde labeling analysis of adult V1, which identified transcriptional signatures of L2/3 glutamatergic neurons that project to the anterolateral (AL) and posteromedial (PM) higher visual areas (HVAs) (Kim et al., 2020; Kim et al., 2018). PM- and AL-projecting neurons localize in the upper and lower regions of L2/3 and express the markers *Cntn5/Grm1* and *Astn2/Kcnh5*, respectively (Figure S6D). In our data, these markers are expressed in a graded and opposite fashion along the pial-ventricular axis, suggesting that PM- and AL-projecting L2/3 neurons localize to the upper (type A) and lower (type C) sublayers, respectively (Figure S6E).

L2/3 neurons form numerous "local" circuits that process diverse visual information, but these are yet to be defined at the cell type level (Harris and Mrsic-Flogel, 2013). While a given excitatory neuron may participate in multiple circuits, there is evidence for synaptic specificity (Kim et al., 2018). It is tempting to speculate that this functional segregation may, in part, be due to graded molecular differences between neurons uncovered in our transcriptomic analysis. These graded differences may also exist along mediolateral and anteroposterior axes to further subdivide V1 into functional circuits.

Experience-dependent cell type specification in L2/3

One of our main findings is that vision specifies L2/3 cell types in V1 and that these cell types are arranged in a sublayered fashion. Recent studies have reported the sublayered organization of cell types in L2/3 of the mouse motor cortex, in addition to the visual cortex (Berg et al., 2021; Gouwens et al., 2019; Munoz-Castaneda et al., 2021; Network, 2021; Scala et al., 2020; Zhang et al., 2021), suggesting an analogous experience-dependent mechanism may be involved in patterning this region. Emerging transcriptomic, morphological, and physiological evidence of similar cell type continuums arranged in sublayers in L2/3 of the human cortex (Berg et al., 2021) raise the exciting possibility that experience-dependent cell-type specification may be a general principle of mammalian cortical development.

Igsf9b is a vision-dependent regulator of cortical circuitry

Patterns of experience-dependent activity may promote the expression of recognition molecules that regulate wiring. Indeed, different patterns of experience-independent activity have been shown to regulate the expression of cell-type specific wiring genes in the mouse olfactory system (Nakashima et al., 2019). Our identification of vision-regulated recognition molecules expressed in L2/3 neurons and genetic studies on *Igsf9b* provide support for the view that experience-dependent processes may also contribute to cell-type specific wiring (Figures 7 and S7).

Analyses of V1 in mice that lack *Igsf9b* revealed changes in inhibitory, but not excitatory, synaptic markers. More significantly, *Igsf9b*$^{-/-}$ mice showed a significant decrease in the proportion of binocular neurons and the proportion of tuned neurons. In the case of the latter phenotype, the severity of the defect increased in deeper sublayers, where in wild type animals, *Igsf9b* expression is higher. A similar impact on the tuning of glutamatergic neurons, more broadly within L2/3, was observed in optogenetic experiments in which perisomatic PV inhibitory neuron activity was suppressed (Zhu et al., 2015). Thus, IGSF9B may modulate PV inhibitory input onto L2/3 excitatory neurons during the critical period. These findings are consistent with previous studies demonstrating a role for IGSF9B in regulating inhibitory synapses.

Limitations of the study

Our data clearly establish that many genes are expressed in a graded fashion along the pial-ventricular axis of L2/3. The simplest interpretation of this finding is that individual cells at different depths express varying ratios of these genes, which would be consistent with the single-cell sequencing data. However, to directly test this hypothesis, future studies should quantify the expression of multiple genes simultaneously in the same cell as a function of the cell's position using spatial transcriptomics methods (Ortiz et al., 2021).

Our single-cell sequencing, FISH, and genetic data support a model in which IGSF9B acts within L2/3 excitatory neurons in a graded fashion to regulate function. This observation mirrors the graded distribution of *Igsf9b* expression along the pial-ventricular axis in L2/3. However, as our deletion of *Igsf9b* was systemic, the precise molecular and cellular mechanisms underlying the phenotype are unclear. Future experiments in this regard would

include inducible, cell-type specific knockouts of *Igsf9b* in L2/3 excitatory neurons, as well as other neuronal populations, with the goal of examining the maturation of L2/3 receptive tuning properties during the critical period. As IGSF9B physically interacts with Negr1 (Wojtowicz et al., 2020), a heterophilic ligand expressed on inhibitory neurons, genetic experiments will be necessary to assess the role of Negr1 in regulating the maturation of L2/3 neurons and to discriminate between a role for IGSF9B-mediated heterophilic versus homophilic interactions in circuit maturation. In a larger context, detailed biochemical, histological, and physiological analyses will be necessary to establish the relationship between the genetic requirement for IGSF9B for the functional maturation of L2/3 neurons and the development of inhibitory synapses.

Concluding Remarks

In summary, our results raise the exciting possibility that experience-dependent cell type specification is a general phenomenon in mammalian brain development. Understanding how the interplay between circuit function, cell type specification, and experience sculpts circuitry will rely on integrating multiple levels of analysis from molecules to behavior.

STAR METHODS

RESOURCE AVAILABILITY

Lead Contact—Further information and requests for resources and reagents should be directed to and will be fulfilled by the Lead Contact, S. Lawrence Zipursky (lzipursky@mednet.ucla.edu).

Materials availability—This study did not generate any new reagents.

Data and code availability

- All raw and processed snRNA-seq datasets reported in this study will be made publicly available via NCBI's Gene Expression Omnibus (GEO) Accession Number GSE190940. Processed h5ad files are available at https://github.com/shekharlab/mouseVC. Visualization of the atlas is available at https://singlecell.broadinstitute.org/single_cell (Study ID: SCP1664). The imaging data has been deposited at https://figshare.com/articles/dataset/Vision-dependent_specification_of_cell_types_and_function_in_the_developing_cortex/16992544.
- Computational scripts detailing snRNA-seq analysis reported in this paper are available at https://github.com/shekharlab/mouseVC. All custom software for imaging analysis will be made available upon request.
- Any additional information required to reanalyze the data reported in this paper is available from the lead contact upon request.

EXPERIMENTAL MODEL AND SUBJECT DETAILS

Mice—Mouse breeding and husbandry procedures were carried out in accordance with UCLA's animal care and use committee protocol number 2009-031-31A, at University

of California, Los Angeles. Mice were given food and water *ad libitum* and lived in a 12-hr day/night cycle with up to four adult animals per cage. Only virgin male C57BL/6J wild-type mice were used for single nuclei sequencing and FISH experiments in this study. For genetic analysis of *Igsf9b*, mice used in immunohistochemistry and 2-photon imaging experiments were naive subjects with no prior history of participation in research studies. All live imaging was performed on mice expressing jGCaMP7f in V1B neurons. GCaMP expression was induced by AAV pGP-AAV-syn-jGCaMP7f-WPRE intracortically injected into Igsf9b WT and KO mice. WT (*Igsf9b*$^{+/+}$) and KO (*Igsf9b*$^{-/-}$) mice were bred from *Igsf9b*$^{+/-}$ mice graciously gifted by the Krueger-Burg lab. These mice were originally obtained by their lab from Lexicon Pharmaceuticals (Thee Woodlands, TX, U.S.A.; Omnibank clon 281214, generated through insertion of the Omnibank gene trap vector 48 into Igsf9b gene in Sv129 ES cells). The commercial version of this mouse has since sold to Taconic Biosciences (1 Discovery Drivee, Suite 304, Rensselaer, NY 12144) (https://www.taconic.com/knockout-mouse/igsf9b-trapped). The mice were backcrossed onto C57BL/6J background for at least 6 generations by the Krueger-Burg lab and confirmed to be null KO in Babaev et al 2018 (https://doi.org/10.1038/s41467-018-07762-1). Genotyping was performed on P6-P9 pups, and genotypes of pups were identified by PCR that was outsourced to Transnetyx (transnetyx.com). Plots for NR and DR mice in Figure 7G, J and K were from unpublished results in Tan et al., 2020. A total of 14 mice, both male (9) and female (5) were used in 2-photon imaging. P21 WT: 3 males and 1 female. P21 KO: 1 male and 2 females. P36 WT: 4 males and 1 female (1 female overlaps with P21 WT). P36 KO: 1 male and 4 females (2 females overlap with P21 KO).

METHODS DETAILS

Visual deprivation experiments—Mice that were dark-reared were done so in a box covered from inside and outside with black rubberized fabric (ThorLabs Cat# BK5) for 7–17 days (P21-P28 or P21-P38) or 9 days (P8-P17) before being euthanized. The dark box was only opened with red light on in the room (mice are more than 10-fold less sensitive to red light). Mice that were dark-light reared were first dark reared for 7 days from P21 to P28 in the dark, and then transferred back to the mouse room to receive 8 hours of ambient light prior to euthanasia. Normally reared mice were housed in a 12 hr light-ON, 12 hr light-OFF cycle. Tissue was collected during a range of 4–8 hours into the light-ON phase. DR mice were dark reared for a period of 7 (P28 DR) and 17 (P38 DR) days with no light. Tissue was collected immediately after retrieving the mice from the dark box. For the dark-light rearing (P28 DL), mice were placed in the light for 8 hours during the light phase in the mouse room after coming out of the dark box.

V1 dissection to obtain single nuclei—Normally-reared mice were dissected at P8, P14, P17, P21, P28, and P38. Isoflurane was used for anesthetization and mice were euthanized by cervical dislocation. Dark-reared mice were dissected at P28 and P38. Dark-light reared mice were dissected at P28 after exposure to 8 hr ambient light. For each age or condition group, 30 mice were dissected: 15 for each biological replicate of single-nucleus(sn) RNA-sequencing. Mice were anesthetized in an isoflurane chamber, decapitated, and the brain was immediately removed and submerged in Hibernate A (BrainBits Cat#

HACA). While the dissection was aimed to target V1b, the region enriched for binocular neurons, due to the small size of this region, the dissection invariably captured neighboring V1 tissue. Therefore, we refer to the tissue as V1. Extracted brains were placed on a metal mold and the slice containing V1 was isolated by inserting one blade 0.5 mm posterior to the lambdoid suture and a second blade 1.5 mm further anterior (2 spaces on the mold). This slice was removed and lowered to Hibernate A in a 60cc petri dish, which was placed on a ruler under a dissecting microscope. The midline was aligned with the ruler and the first cut was bilaterally 3.3 mm out from the midline. The second cut was 0.7 mm medial to the first cut. The cortex was peeled off the underlying white matter. The V1 piece with a total of 1 mm cortex depth by 1.5 mm thickness was transferred to a dish containing 600 μl of RNAlater (Thermo Fisher Cat# AM7020) and kept on ice until dissections were complete. Dissected tissues were then kept in RNAlater at 4°C overnight and transferred to −20°C the next day. Tissue was stored this way for up to 1 month prior to being processed for snRNA-seq.

Droplet-based single-nucleus(sn) RNA-sequencing—For each biological replicate, dissected V1 regions from 15 mice were removed from RNAlater, weighed, then chopped with a small blade on a cleaned slide on top of a cooling cube. Tissue was then transferred to a dounce homogenizer chilled to 4°C and denounced slowly 30 times with a tight pestle in 1 ml of homogenization buffer containing 250mM Sucrose, 150mM KCl, 30mM $MgCl_2$, 60mM Tris pH 8, 1 μM DTT, 0.5x protease inhibitor (Sigma-Aldrich Cat# 11697498001), 0.2 U/μl RNase inhibitor, and 0.1%TritonX. All solutions were made with RNase-free H2O. Each sample was filtered through a 40 μm cell strainer and then centrifuged at 1000g for 10 minutes at 4°C. The pellet was resuspended in the homogenization buffer and an equal volume of 50% iodixanol was added to the resuspended pellet to create 25% iodixanol and nuclei mix. This mix was layered upon 29% iodixanol and spun at 13,500g for 20 minutes at 4°C. The supernatant was removed and the pellet was washed in a buffer containing 0.2 U/μl RNAse inhibitor, PBS (137 mM NaCl, 2.7 mM KCl, 8 mM Na_2HPO_4, and 2 mM KH_2PO_4, pH 7.4), 1% bovine serum albumin, and then filtered over a 40 μm filter and centrifuged at 500g for 10 minutes at 4°C. The pellet was resuspended and filtered with two more 40 μm filters, cells counted on a hemocytometer and then diluted to 700–1200 nuclei/mm^3. Nuclei were re-counted on a 10X automated cell counter. Nuclei were further diluted to the optimal concentration to target capturing 8000 cells per channel.

Nuclei from each biological replicate were split into two and run separately on two channels of 10X v3, targeting 8,000 cells per channel. We refer to these as library replicates. For each experiment, we performed two biological replicates towards a total of four library replicates. The two biological replicates were processed on different days. Sequencing was performed using the Illumina NovaSeq™ 6000 Sequencing System (S2) to a depth of ~30,000 reads per cell. All library preparation and sequencing were performed at the UCLA's Technology Center for Genomics & Bioinformatics (TCBG) core.

Single-molecule fluorescent *in situ* hybridization (smFISH)—C57/BL6J mice were anesthetized in isoflurane at ages ranging from P8 to P38 and then perfused transcardially with heparinized PBS followed by 4% paraformaldehyde (PFA) diluted in

PBS and adjusted to pH 7.4. Following perfusion, the brains were collected and postfixed for 24h at 4°C in 4% PFA, and then cryoprotected sequentially in 10%, 20%, and 30% sucrose in PBS solution until the brain sank. Brains were then frozen in OCT using a methylbutane and dry ice bath and stored at −80°C until time of sectioning. Brains were cut into 15 μm thick coronal sections at −22/−20°C using a cryostat (Leica CM 1950) and single sections were collected in a charged microscope slide in ascending order from the frontal to the occipital region starting in V1. For localization of the visual cortex V1 and binocular zone of V1, coordinates from (Franklin, 2012) were used. Sections were stored at −80°C until further processing. For all FISH experiments, coronal sections were selected to be from a similar anatomical region within V1 when comparing conditions or ages.

Multiplex FISH was performed following ACD Biology's Multiplex RNAscope v2 assay (Advanced Cell Diagnostics, cat# 323110). Briefly, thawed sections were baked at 60°C, post-fixed for 1 hr at 4°C in 4% PFA, and then dehydrated in sequential ethanol treatments followed by H_2O_2 permeabilization and target retrieval. Protease III treatment was used, then application of probes and sequential amplification and fluorophore development fluorophores (Akoya Biosciences cat# FP1487001KT, FP1488001K, FP1497001KT). Slides were counterstained with 1 ug/ml 4,6-diamidino-2-pheenylindole (DAPI, Sigma cat #D9542) and mounted with Prolong Gold (Thermo Fisher Scientific cat# P36930). RNAscope probes used include: *Igsf9b* (cat# 832171-C3), *Mdga1* (cat#546411, 546411-C2), *Nlgn2* (cat# 406681). Cdh13 (cat # 443251-C3), *Chrm2* (cat # 495311-C2), *Deptor* (cat #481561 - C3), *Gad1* (cat3 400951-C2), *Slc17a7* (cat# 416631-C2, 416631, 416631-C3), *Trpc6* (cat# 442951), *Tshz2* (cat# 431061-C1). Each time point or condition had three to four biological replicates comprising brain sections from different mice. NR mice at P8, P14, P17, P21, P28, and P38, DR mice at P17, P28, and P38, and DL mice at P28 were used.

Immunolabeling for synaptic markers—Immunolabeling for VGLUT1 and GAD65 on brains at all time points shown was performed on perfusion-fixed brains that underwent the same preparation as for smFISH. Brains were sectioned to 15 μm sections. Sections were then incubated for 24 hr with anti-VGLUT1 (guinea pig polyclonal Millipore Sigma Cat# AB5905) and anti-GAD65 (mouse monoclonal Millipore Sigma Cat#MAB3521R) diluted 1:500 in blocking solution (10% NGS in 0.3% PBST), washed 3x times in PBS, and then incubated for 2 hr with goat anti-mouse 488 (Invitrogen Cat# A11029) and goat anti-guinea pig 568 (Invitrogen Cat#A11075) both diluted 1:500 in blocking solution.

Immunolabeling for synaptic markers in IGSF9B KO vs WT experiments were performed on perfusion-fixed brains sectioned to 40 μm and preserved in aliquots of antifreeze (42.8g Sucrose Fisher Cat # S25590B, 0.33g of MgCl2.6H2O Sigma Cat#M2670, 312.5g (250 mL) glycerol Sigma Cat#G7757, 25mL 10X PBS, total to 500 mL w/ddH2O). On the day of the experiment, tissues were washed 4 times at 15 minutes per wash from antifreeze using 0.3% PBST, blocked with 10% goat serum in PBST, incubated with primary antibody at 4C for 2 nights (~44 hours). Samples were washed 4 times, 15 minutes each in 1X PBS, then secondary antibody diluted in blocking solution was added for 2 hr at room temperature. Samples were washed 4 times at 10minutes per wash in 1X PBS then stained with 1:10k DAPI for 15 minutes, washed for 10 min in PBS, and then mounted with Prolong Gold. Primary antibodies used include: anti-VGLUT1 (guinea pig

polyclonal Millipore Sigma Cat# AB5905), anti-VGLUT2 (Guinea pig polyclonal Synaptic Systems Cat#135404, anti-GAD65 (mouse monoclonal Millipore Sigma Cat#MAB3521R), anti-NLGN2 (guinea pig polyclonal Synaptic Systems Cat#129205), anti-GABRA1 (rabbit polyclonal Synaptic Systems Cat#224203), anti-GABRG2 (guinea pig polyclonal Synaptic Systems Cat#224004 (anti-GPHN (mouse monoclonal Synaptic Systems Cat#147011), anti-VGAT (rabbit polyclonal Synaptic Systems Cat#131002), anti-PSD95 (rabbit polyclonal Invitrogen Cat#VH307495), anti-SSCAM (rabbit polyclonal Sigma Aldrich Cat#2441). Secondary antibodies used include goat anti-guinea pig 566 (Invitrogen Cat#A11075), goat anti-guinea pig 647 (Life Technologies Cat#A21450), goat anti-mouse 488 (Invitrogen Cat#A11029), goat anti-guinea pig 568 (Invitrogen Cat#A11075), goat anti-rabbit 488 (Life Technologies Cat#A11008), goat anti-mouse 568 (Invitrogen Cat#A11031), goat anti-rabbit 647 (Invitrogen Cat#A21244), goat anti-rabbit 568 (Invitrogen Cat#A11011).

Confocal imaging—All histology images were acquired on a Zeiss LSM 880 confocal microscope with Zen digital imaging software. *In situ* hybridization images were acquired using 20x and 40x magnification objectives with 0.8 NA and 1.2 NA, respectively. Each image frame was 1024 pixels × 1024 pixels. For 20X and 40X images, this corresponded to a 425.1 μm × 425.1 μm and 212.5 μm × 212.5 μm coverage area per frame, respectively. Vertically tiled 20X images were acquired covering all cortical layers, as well as 40X horizontal tiled images to cover L2/3 only. Z-stacks were taken to cover the entire 15 μm section. *Mdga1* and *Ccbe1,* both L2/3-markers, were used as markers to assess the cortical depth covered by each 40X image. For each 40X frame starting at layer 2, one frame covered the depth of L2/3 based on *Mdga1* and *Ccbe1* signals.

For immunolabeling experiments of synaptic markers, images were taken using a confocal microscope with high NA 63X magnification objective (1.4 NA), imaged on both hemispheres of the brain in L2/3 of V1 based on anatomical landmarks. Each z-stack comprising 15 optical sections spanned the first 5 μm of each section imaged with step interval of 0.3648 μm. For thick (40 μm) immunohistochemical sections, two 5 μm thick z-stacks under 63X objective were vertically tiled to cover the entire L2/3 of V1. Each individual imaging frame is 1024×1024 in pixel with 134.95 μm × 134.95 μm area coverage; two tiled images result in a final area coverage of 134.95 μm × 269.9 μm.

Imaging quantification—3D z-stacked images were z-projected on FIJI version 2.1.0/1.53c. The entire z-stack covering the slide was projected into a 2D image with maximum intensity. 20X images were tiled using DAPI and *Slc17a7* channels (when available) as guides through linear blending to capture the entire cortical thickness. 40X and 63X images were processed as is. Maximum-projected images were entered into CellProfiler using a custom pipeline modified from the original SABER-FISH pipeline (Kishi et al., 2019). Modifications were made to detect up to four imaging channels (McQuin et al., 2018). CellProfiler was used to perform nuclear and cell segmentation, as well as puncta counting. Nuclear segmentation was done by using DAPI and cellular segmentation was done by taking a fixed radius of 5 pixels around the nucleus. For downstream computation, nuclear segmentation results were used. Segmented images had nuclear boundaries as well

as individual puncta married in an overlay color with original image items in gray. All segmented images were inspected to ensure no aberration in segmentation or puncta calling.

After segmentation and puncta calling, data were analyzed in R using custom scripts to compare nuclear mRNA counts (i.e., number of puncta) between time points and conditions. For cell type experiments, cells were sorted into types based on mRNA counts of marker genes. Briefly, cells were ranked based on their mRNA counts of each gene and visualized as a scatter plot of counts vs. rank. The knee of this plot was located (Arneson et al., 2018). The mRNA count value at the knee was chosen as the cutoff for cell type assignment. Quantification of protein puncta in immunolabeling experiments also used Cell Profiler by adapting the same pipeline developed to count mRNA puncta. Protein puncta were quantified per image and normalized by the number of nuclei segmented in that image (Figure S7B–F). In Figure S7G, the unique peri-nuclear somatic distribution of NLGN2 enabled its quantification using a 20-pixel boundary around the nucleus and counting the puncta that fell in that boundary. This allowed for quantifying NLGN2 protein puncta per cell.

Surgery and AAV injection—All epifluorescence and two-photon imaging experiments were performed through chronically implanted cranial windows. Mice aged P10–11 (for P21 imaging) or P25–26 (for P36 imaging) were administered with carprofen analgesia prior to surgery, anesthetized with isoflurane (5% for induction; 0.75–1.5% during surgery), mounted on a stereotaxic surgical stage via ear bars and a mouth bar. Their body temperature was maintained at 37°C via a heating pad. The scalp and connective tissue were removed, and the exposed skull was allowed to dry. Then a thin layer of Vetbond was used to cover the exposed skull and wound margins. Once dry, a thin layer of dental acrylic was applied around the wound margins, avoiding the region of skull overlying V1. A metal head bar was affixed with dental acrylic caudally to V1. A 3mm circular piece of skull overlying binocular V1 on the left hemisphere was removed after using high-speed dental drill to thin the bone along the circumference of this circle. Care was taken to ensure that the dura was not damaged at any time during drilling or removal of the skull.

Local AAV injection into binocular V1 took place after the skull was removed. Exposed brain was submerged in normal saline during injection. AAV was diluted in 1xPBS that contains 2.5% mannitol (w/v) to a final titer of $6.7\sim7.5\times10^{12}$ genomes per ml. Mannitol was used to increase the viral spread (Mastakov et al., 2001). For both age groups, virus was injected at least 10 days before imaging. Virus injection was done using a glass micropipette (tip diameter: 19–25 μm) and Nanoject III (Drummond Scientific Company) attached on Scientifica PatchStar Micromanipulator (Scientifica) controlled with LinLab2 (Scientifica). Injection site was at 3 mm lateral from the midline and 1 mm rostral from lambda. Injections occurred at three depths: 470, 340 and 210 μm below the pial surface. At each depth, 65 cycles of injection were done, with each cycle injecting 5 nL at 5 nL/s speed, with 10 second intervals between cycles. Thus, 325 nL of AAV was injected at each depth, and 975 nL was injected into V1B in total. After virus injection, a sterile 2.5 mm diameter cover glass was placed directly on the exposed dura and sealed to the surrounding skull with Vetbond. The remainder of the exposed skull and the margins of the cover glass were sealed with dental acrylic. Mice were then recovered on a heating pad. When alert, they were placed back in

their home cage. Carprofen was administered daily for 3 days post-surgery. Mice were left to recover for at least 10 days prior to imaging. Mice injected at P10–11 would also be imaged at P36 if their cranial windows remained clear.

Mapping of binocular area of the primary visual cortex—The precise location of the binocular region in V1 on the left hemisphere for each mouse was identified using low magnification, epifluorescence imaging of jGCaMP7f signals. For all mice, visual areas were mapped the day before imaging. Briefly, jGCaMP7f was excited using a 470nm light-emitting diode. A 27-inch LCD monitor (ASUS, refreshed at 60 Hz) was positioned such that the binocular visual field fell in the center of the monitor. The screen size was 112 deg in azimuth and 63 deg in elevation and the monitor was placed 20 cm from the eyes. A contrast reversing checkerboard (checker size 10×10 degree) bar windowed by a 1D Gaussian were presented along the horizontal or vertical axis to both eyes (Figure S7H). The checkerboard bar drifted normal to its orientation and swept the full screen width in 10 sec. Both directions of motion were used to obtain an absolute phase map along the two axes. Eight cycles were recorded for each of the four cardinal directions. Images were acquired at 10 frames per second with a PCO edge 4.2 sCMOS camera using a 35mm fixed focal length lens (Edmund optics, 35mm/F1.65, #85362, 3mm field of view). The camera focused on the pial surface. The visual areas were obtained from retinotopic maps of azimuth and elevation. The binocular area of the primary cortex was defined as the region of primary visual cortex adjacent to the higher visual area LM (Figure S7I).

Two-photon calcium imaging—Two-photon imaging was targeted to the binocular area of V1 using a resonant/galvo scanning two-photon microscope (Neurolabware, Los Angeles, CA) controlled by Scanbox image acquisition software (Los Angeles, CA). A Coherent Discovery TPC laser (Santa Clara, CA) running at 920 nm focused through a 16x water-immersion objective lens (Nikon, 0.8 numerical aperture) was used to excite jGCaMP7f. The objective was set at an angle of 10–11 degrees from the plumb line to reduce the slope of the imaging planes. Image sequences (512×796 pixels, 490×630 μm) were captured at 15.5 Hz at a depth of 120 to 320μm below the pial surface on alert, head-fixed mice that were free to run on a 3D-printed running wheel (14cm diameter). A rotary encoder was used to record the rotations of this running wheel. Three planes that were well separated in depth and covered the top, middle and bottom of L2/3 were imaged per mouse (Figure S7J). To measure responses of neurons to each eye separately, an opaque patch was placed immediately in front of one eye when recording neuronal responses to visual stimuli presented to the other eye.

Visual stimulation during 2-photon imaging—On the same screen that was used for visual area mapping, a set of sinusoidal gratings with 18 orientations (equal intervals of 10 degrees from 0 to 170 degrees), 12 spatial frequencies (equal steps on a logarithmic scale from 0.0079 to 0.1549 cycles per degree) and 8 spatial phases were generated in real-time by a Processing sketch using OpenGL shaders (see https://processing.org). These static gratings were presented at 4 Hz in full screen in pseudo-random sequence with 100% contrast (Figure 7A). Imaging sessions were 15 min long (3600 stimuli in total), thus each combination of orientation and spatial frequency appeared 16 or 17 times. Transistor-

transistor logic signals were used to synchronize visual stimulation and imaging data. The stimulus computer generated these signals, and these were sampled by the microscope electronics and time-stamped by the acquisition computer to indicate the frame and line number being scanned at the time of the TTL.

Analysis of two-photon imaging data

Image processing: Movies for either eye from the same plane were processed together using a standard pipeline consisting of movie concatenation, motion correction, cell segmentation and ROI signal extraction using Suite2p (https://suite2p.readthedocs.io/). ROIs determined for each experiment were inspected and confirmed visually (Figure S7K). Neuronal spiking was estimated via non-negative temporal deconvolution of the extracted ROI fluorescence signal using Vanilla algorithm (Figure S7L) (Berens et al., 2018). Subsequently, fluorescent signals and estimated spiking for each cell were split into separate files corresponding to the individual imaging session for each eye. Each imaging plane was processed independently.

Calculation of response properties

Identification of visually responsive neurons using SNR: Signal to noise ratio (SNR) was used to identify neurons with significant visual responses (tuned neurons). SNR for each neuron was calculated based on the optimal delay of the neuron. Optimal delay was defined as the imaging frame after stimulus onset at which the neuron's inferred spiking reached maximum. To calculate SNR, signal was the mean of standard deviations of spiking to all visual stimuli around the optimal delay (4–6 frames, thus ~0.323 sec, after stimulus onset; see Figure 7H), and noise was this value at frames well before or after stimulus onset (frames −2 to 0, and 13 to 17). Neurons whose optimal delays occurred outside of the time-locked stimulus response window of 3 to 7 frames after stimulus onset (padded by ±1 frame around the 4–6 frame range used above) were spontaneously active but visually unresponsive. They were untuned neurons and had SNR values close to 1 (Figure 7I). The SNR values of these untuned neurons were normally distributed (mean = 1.0±0.03) over a narrow range. Untuned neurons with optimal delays naturally occurring in the 3–7 frame time window can be distinguished from visually responsive neurons by SNR. This SNR threshold was defined at 3 standard deviations above the mean SNR of the above-mentioned normal distribution (See the vertical dashed lines in Figure 7K). SNR values were calculated separately for responses to the ipsilateral or contralateral eye. A neuron is monocular if its SNR for one eye, but not the other, was above the threshold (Figure 7C). A neuron is binocular if its SNR for either eye was above the threshold (Figure 7D). A neuron is untuned if its SNR for neither eye was above the threshold.

Tuning kernel for orientation and spatial frequency.: The estimation of the tuning kernel was performed by fitting a linear model between the response and the stimulus. Cross-correlation maps were used to show each neuron's inferred spiking level to each visual stimulus (orientation and spatial frequency) and were computed by averaging responses over spatial phases. The final tuning kernel of a neuron was defined as the correlation map at the optimal delay (Figure 7B).

Orientation preference.: We used vertical slices of the tuning kernel through the peak response and calculated the center of mass of this distribution as orientation preference. Orientation preference calculation:

$$Orientation = \frac{arctan\left(\sum_n O_n e^{i2\pi\theta_n/180}\right)}{2}$$

O_n is a 1×18 array, in which a level of estimated spiking (O_1 to O_{18}) occurs at orientations θ_n (0 to 170 degrees, spaced every 10 degrees). Orientation is calculated in radians and then converted to degrees.

ΔOrientation for binocular neurons.: For a binocular neuron, Ori_{contra} is the neuron's orientation preference to contralateral eye and Ori_{ipsi} is the orientation preference to ipsilateral eye. $\Delta Orientation$ was calculated as

$$\Delta Orientation = |Ori_{contra} - Ori_{ipsi}|$$

If the value of $\Delta Orientation$ is above 90 (e.g., |170–10|=160), then the actual value for the difference of orientation preferences to two eyes is 180- $\Delta Orientation$ (180–160=20).

Quantification and Statistical Analysis for 2-photon imaging: A power analysis was not performed a-priori to determine sample size. All statistical analyses were performed in MATLAB (https://www.mathworks.com/), using non-parametric tests with significance levels set at $\alpha < 0.05$. Bonferroni corrections for multiple comparisons were applied when necessary. Mann-Whitney U-tests (Wilcoxon rank sum test) or two-sample Kolmogorov-Smirnov tests were used to test differences between two independent populations.

Computational analysis of single-nucleus transcriptomics data

Alignment and quantification of gene expression: Fastq files with raw reads were processed using Cell Ranger v3.1.0 (10X Genomics) with default parameters. The reference genome and transcriptome used was GRCm38.92 based on Ensembl 92, which was converted to a pre-mRNA reference package by following Cell Ranger guidelines. Each single-nucleus library was processed using the same settings to yield a gene expression matrix (GEM) of mRNA counts across genes (columns) and single nuclei (rows). Each row ID was tagged with the sample name for later batch correction and meta-analysis. We henceforth refer to each nuclear transcriptome as a "cell."

Initial pre-processing of normally reared samples to define classes, subclasses, and types: This section outlines the initial transcriptomic analysis of data from normally reared samples. Unless otherwise noted, all analyses were performed in Python using the SCANPY package (Wolf et al., 2018). The complete computational workflow is illustrated in Figure S1D.

1. Raw GEMs from 23 snRNA-seq libraries were combined: 6 ages, 2 biological replicates per age and 2 library replicates per biological replicate except for P38,

where one of the technical replicates failed quality metrics at the earliest stage of processing. This resulted in a GEM containing 184,936 cells and 53,801 genes.

2. We then generated scatter plots of the number of transcript molecules in each cell (n_counts), the percent of transcripts derived from mitochondrially encoded genes (percent_mito), and the number of expressed genes (n_genes) to identify outlier cells. Cells that satisfied the following conditions were retained: 700 < n_genes < 6500, percent_mito < 1%, and n_counts < 40,000. Only genes detected in more than 8 cells were retained for further analysis. This resulted in a GEM of 167,384 cells and 30,869 genes.

3. Cells were normalized for library size differences. Transcript counts in each cell were rescaled to sum to 10,000 followed by log-transformation. For clustering and visualization, we followed steps described previously (Peng et al., 2019). Briefly, we identified highly variable genes (HVGs), z-scored expression values for each gene, and computed a reduced dimensional representation of the data using principal component analysis (PCA). The top 40 principal components (PCs) were used to compute a nearest-neighbor graph on the cells. The graph was then clustered using the Leiden algorithm (Traag et al., 2019) and embedded in 2D via the Uniform Manifold Approximation and Projection (UMAP) algorithm (Becht et al., 2018).

Additional filtering and class assignment: The analysis above yielded 42 clusters (Figures S1E–F). Canonical marker genes for cortical classes and subclasses were used to annotate these clusters (Figure S1G, Table S1). We then used Scrublet (Wolock et al., 2019) to identify doublets (Figure S1H). Clusters that expressed markers of two or more classes or contained more than 50% doublets were labeled “Ambiguous” (Figure S1I). Removal of ambiguous clusters and doublets in the dataset resulted in a GEM containing 147,236 cells by 30,868 genes.

For further analysis, this matrix was subsetted by cell class (glutamatergic neurons, GABAergic neurons, and non-neuronal cells) and age (P8, P14, P17, P21, P28 and P38) into 18 separate GEMs (Figure S1D).

Identification of cell types within each class by age: Each of the 18 GEMs were separately clustered using the procedure described above with one modification. Following PCA, we used Harmony (Korsunsky et al., 2019) to perform batch correction. The nearest-neighbor graph was computed using the top 40 batch-corrected PCs.

Each GEM was then iteratively clustered. We began by clustering cells using the Leiden algorithm, with the resolution parameter fixed at its default value of 1. As before, UMAP was used to visualize the clusters in 2D. Through manual inspection, small clusters with poor quality metrics or ambiguous expression signatures were discarded, likely representing trace contaminants that escaped detection in the earlier steps. The remaining clusters were annotated by subclass based on canonical expression markers (Table S1, Figure 1D). Next, we performed a differential expression (DE) analysis between each cluster and other clusters in its subclass. If a cluster did not display unique expression of one or more genes, it was

merged with the nearest neighboring cluster in the UMAP embedding as a step to mitigate over-clustering. This DE and merging process was repeated until each cluster had at least one unique molecular signature (Figures S3A–C). We refer to the final set of clusters as types.

Workflow for supervised classification analyses: To assess transcriptomic correspondence of clusters across ages or between rearing conditions, we used XGBoost, a gradient boosted decision tree-based classification algorithm (Chen and Guestrin, 2016). In a typical workflow, we trained an XGBoost (version 1.3.3) classifier to learn subclass or type labels within a "reference" dataset, and used it to classify cells from another, "test" dataset. The correspondences between cluster IDs and classifier-assigned labels for the test dataset are used to map subclasses or types between datasets. The classification workflow is described in general terms below and applied to various scenarios in subsequent sections.

Let R denote the reference dataset containing N_R cells grouped into r clusters. Let T denote the test dataset containing N_T cells grouped into t clusters. Here, each cell is a normalized and log-transformed gene expression vector $\boldsymbol{u} \in R$ or $\boldsymbol{v} \in T$. The length of $\boldsymbol{u}$ or $\boldsymbol{v}$ equals the number of genes. Based on clustering results, each cell in R or T is assigned a single cluster label, denoted cluster($\boldsymbol{u}$) or cluster($\boldsymbol{v}$). cluster($\boldsymbol{u}$) may be a type or subclass identity, depending on context.

The main steps are as follows:

1. We trained multi-class XGBoost classifiers $C_R{}^0$ and $C_R{}^T$ on R and T independently using all 30,868 genes as features. In each case, the dataset was split into training and validation subsets. For training we randomly sampled 70% of the cells in each cluster, up to a maximum of 700 cells per cluster. The remaining "held-out" cells were used for evaluating classifier performance. Clusters with fewer than 100 cells in the training set were upsampled via bootstrapping to 100 cells in order to improve classifier accuracy for the smaller clusters. Classifiers achieved a 99% accuracy or higher on the validation set. XGBoost parameters were fixed at the following values:
    1. 'Objective': 'multi:softprob'
    2. 'eval_metric': 'mlogloss'
    3. 'Num_class': r (or t)
    4. 'eta': 0.2
    5. 'Max_depth': 6
    6. 'Subsample': 0.6
2. When applied to a test vector $\boldsymbol{c}$, the classifier $C_R{}^0$ or $C_R{}^T$ returns a vector $p = (p_1, p_2, \ldots)$ of length r or t, respectively. Here, p_i represents the probability value of predicted cluster membership within R or T, respectively. These values are used to compute the "softmax" assignment of $\boldsymbol{c}$, such that cluster($\boldsymbol{c}$) = $arg\ max_i$

p_i if $arg\ max_i\ p_i$ is greater than $1.2*(1/r)$ or $1.2*(1/t)$. Otherwise $\boldsymbol{c}$ is classified as 'Unassigned'.

3. Post training, we identified the set of top 500 genes based on average information gain for each $C_R{}^0$ and $C_R{}^T$. These gene sets are denoted G_R and G_T.

4. Using the common genes $G = G_R \cap G_T$, we trained another classifier C_R on 70% of the cells in R, following the procedure outlined in 1. As before, the performance of C_R was evaluated on the remaining 30% of the data.

5. Finally, we trained a classifier C_R on 100% of the cells in R. C_R was then applied to each cell $\boldsymbol{v} \in T$ to generate predicted labels cluster($\boldsymbol{v}$).

Comparing transcriptomic signatures of developmental V1 to adult V1/ALM subclasses (Tasic et al., 2018): We used the aforementioned classification workflow to evaluate the correspondence between V1 subclasses in this work (Figure 1D) and those reported in a recent study of the adult V1 and motor cortex (ALM) (Tasic et al., 2018). We trained a classifier on the V1/ALM subclasses and used it to assign an adult label to each V1 cell collected in this study. A confusion matrix was used to visualize the correspondence between developmental V1 subclasses and V1/ALM subclasses at adulthood (Figure S1J). This correspondence served as a proxy to evaluate the overall conservation of subclass-specific transcriptomic signatures across developmental stages (developing vs. adult), RNA source (single-nucleus vs. single-cell), platform (3' droplet-based vs. full-length plate-based), and region (V1 vs. V1/ALM).

Inferring temporal association between V1 types using supervised classification

Relating types across time: The supervised classification workflow was used to relate cell types identified at each pair of consecutive ages within each class (5 × 3 = 15 independent analyses). In each case, the classifier was trained on the older age dataset and applied to each cell in the younger age dataset. Thus, each cortical cell at the younger age possessed two type labels, one identified via clustering of cells at that age and the other based on a classier trained at the next age. Assessing the correspondence between these labels enabled us to link cell types between consecutive ages (e.g., P8-P14, P14-P17 and so on) and track their maturation across development

Quantification and visualization of cluster correspondence: The correspondences between types throughout development were visualized using Sankey flow diagrams (Figures 2E, S2F–G). In the case of glutamatergic neurons, for example, inspecting the Sankey flow diagrams revealed that L2/3 and 4 types mapped more diffusely across time than L5 and 6 types, suggesting subclass specific differences in maturation. We quantified such subclass-specific differences using three methods,

1. We computed the adjusted rand index (ARI) between the cluster labels and classifier-assigned labels. The ARI ranges from 0 and 1, with extremes corresponding to random association and perfect (i.e., 1:1)

mapping, respectively. Negative values are possible for the ARI but were not observed in our data. The ARI was computed using the function sklearn.metrics.adjusted_rand_score(). ARI values were computed for each pair of consecutive ages (e.g., P8 and P14) within each subclass (e.g., L2/3). ARI differences between glutamatergic subclasses were visualized as bar plots (Figure 2F). The analysis was repeated for GABAergic and non-neuronal cells (Figure S2H–I).

2. We computed for each type the F1 score, which is a measure of a classifier's effectiveness at associating cells within a type to their correct type label. Its value ranges from 0 to 1, with extremes corresponding to no association and perfect association between transcriptome and type label, respectively. The F1 score was computed for each type at each time point using the function sklearn.metrics.f1_score(). Values were grouped by subclass to visualize differences (Figures S2J–L). This analysis showed that in addition to exhibiting poor temporal correspondence, L2/3 and L4 types were also less transcriptomically distinct than L5 and L6 types at any given time point (Figure S2J). Subclasses within GABAergic and non-neuronal cells did not exhibit such striking differences (Figures S2K–L).

3. We assessed the sensitivity of each subclass' clustering results to the clustering resolution parameter of the Leiden algorithm, which controls the number of output clusters. The clustering resolution was increased from 1 to 2. We computed the ARI between the clusters identified at each value of the resolution parameter and the baseline clusters computed at a resolution value of 1. The ARI was computed for the clusters within each subclass at each time point separately. L2/3 and L4 clustering was more sensitive to changes in the resolution parameter than the clustering in L5 and L6 (Figure 2G).

Analysis of visual deprivation experiments

Separation of major cell classes: In visual deprivation experiments, snRNA-seq profiles were collected from cortical samples of mice dark-reared from P21-P28 (P28DR), dark-reared from P21-P38, (P38DR) and dark-reared from P21-P28 followed by 8 hours of ambient light stimulation. Overall, 12 GEMs from these three experiments were combined and preprocessed (4 libraries per experiment) using the steps described above for normally reared samples. The numbers of cells prior to pre-processing were 43,234, 36,373 and 31,815 for P28DR, P38DR and P28DL respectively. The final numbers of high-quality cells reported were 24,817, 25,671, and 26,575, respectively.

Comparing DR and DL clusters to NR types using supervised classification: To examine cell type correspondence between visual deprivation and normally reared experiments, we used supervised classification as described above. Classifiers were trained on P28NR and P38NR types, and cells from P28DL, P28DR, and P38DR were mapped to the corresponding NR age. The resulting confusion matrices were visualized as dot plots, and the ARI was computed for types within each subclass (Figure S5).

Differential gene expression analysis: Differential expression (DE) was performed in multiple settings to identify genes enriched in specific classes, subclasses, types, or rearing conditions. We used the scanpy.tl.rank_genes_groups() function and Wilcoxon rank-sum test in the scanpy package for statistical comparisons (Wolf et al., 2018). While searching for genes enriched in a particular group of interest, only those expressed in >20% of cells in the tested group were considered.

The results of the DE analyses were used in the following contexts: 1) To assess the quality of cell populations identified in the initial analysis, where each cluster in Figure S1F was compared to the rest. Clusters that did not express a unique signature or those that express markers known to be mutually exclusive were removed; 2) To identify subclass markers (Figure 2B, Figure S2D–E). This was accomplished by comparing each subclass against the rest; 3) To identify type-specific markers within each subclass (Figure S3A–C). Here, each type was compared to other types of the same subclass; and 4) To identify gene expression changes as a result of visual deprivation. We performed DE between NR and DR (both ways) subclasses (Figure 6A, Figure S6A).

Identification of genes showing graded expression among L2/3 types: We compared each L2/3 type to the other two (e.g., A vs B and C) to identify 287 type-specific genes at fold change > 2 and p-value < 10^{-10} (Wilcoxon test). The expression levels of these genes were z-scored, and we used *k*-means clustering to identify k=7 groups based on their pattern of expression among the three types (Figure S6A). The optimal number of groups was identified using the elbow method. Five of the seven groups, containing 217 genes, showed graded expression differences that could be classified into one of the following patterns based on visual inspection: A > B > C (77 genes), A < B > C (36 genes), C > A > B (9 genes), C > B > A (85 genes) and A > C > B (10 genes). The remaining X genes were expressed in a digital fashion that fell into one of two groups: C > B = A (35 genes) and A > B = C (35 genes). Thus, approximately 75% of the DE genes among L2/3 types are expressed in a graded fashion.

Pseudo-spatial inference of gene expression in L2/3: FISH experiments targeting the three L2/3 glutamatergic type markers revealed that type A resides at the top (near the pia), type B in the middle, and type C at the bottom of L2/3, bordering L4 (Figure 3). Surprisingly, this relative positioning of A, B, and C types was mirrored in the UMAP embedding. We therefore hypothesized that the UMAP coordinates of a neuron may serve as a proxy for the approximate relative position of its soma in the tissue and used this to calculate the expected spatial expression profiles of genes in each dataset.

In a given scenario, we marked the “A” and “C” cells furthest from each other on the UMAP space as the “root” and the “leaf” and assumed that these represent the top and bottom of L2/3 respectively. We used diffusion pseudo-time (DPT) (Haghverdi et al., 2015; Wolf et al., 2019) to order all L2/3 cells relative to the root cell. DPT and similar methods have been used previously to order cells based on their developmental state (i.e., pseudo-time); we have used it in this context to infer “pseudo-spatial” position based on the observed correspondence described above. Pseudo-spatial positions for cells were close to 0 at the top, where type A begins, and gradually increased through types B and C, reaching the maximum

normalized value of 1 at the end of L2/3 in UMAP space. We performed this pseudo-spatial analysis for L2/3 neurons in each of the six normally reared samples.

For the DR and DL datasets, where the spatial organization and transcriptomic profiles are disrupted, a root cell was randomly selected from the beginning of L2/3 in UMAP space (e.g., a cell from the edge of cluster "L2/3_1" was chosen for P28DR) (Figure 4B). Finally, to visualize the expression of gradient genes as a function of pseudo-spatial position (Figure 6F, H), we averaged the expressions along bins of pseudo-spatial location that contained as many cells as ~10% of a given dataset.

Identification of temporally regulated genes: This analysis was repeated separately for each of L2/3, L4, L5, and L6. Of the 30,868 genes in the data, we considered only those expressed in more than 20% of the cells in at least one of the six time points. This resulted in 6339, 5746, 6096, and 5428 genes for further analysis in L2/3, L4, L5, and L6, respectively. We first computed the average expression strength of every gene at each of the six time points. Here, the average expression strength $E_{g,t}$ of gene g at age t is defined as follows,

$$E_{g,t} = F_{g,t} X_{g,t}$$

where $F_{g,t}$ is the fraction of cells at age t that express gene g and $X_{g,t}$ is the mean transcript counts of g among cells with non-zero expression. We only considered genes that satisfied the following condition,

$$\frac{\max\left(E_{g,t}\right) - \min\left(E_{g,t}\right)}{\max\left(E_{g,t}\right)} \geq 0.3$$

resulting in 2594, 2410, 2190, and 2192 genes for further analysis in L2/3, L4, L5, and L6, respectively. Next, to identify genes that showed significant temporal variation, we z-scored each E_g vector and randomly shuffled the temporal identities of the cells. We then recomputed a randomized analog of $E_{g,t}$, which we call $\widehat{E_{g,t}}$. We then defined for each gene g a deviation score between the actual and randomized expression vectors,

$$\alpha_g = \frac{\sum_t^{\mathrm{T}} \left(E_{g,t} - \widehat{E_{g,t}}\right)^2}{\sqrt{\sum_t^{\mathrm{T}} E_{g,t}^2 \sum_t^{\mathrm{T}} \widehat{E_{g,t}^2}}}$$

Here, $T = 6$ is the number of time points and the denominator acts as a normalizing factor; we observed a bias towards highly expressed genes in its absence. High values of α_g indicate that the observed temporal pattern of expression is significantly different from the randomized pattern. We picked 855 genes for further analysis that had $\alpha_g > 0.2$. This threshold was chosen by computing an empirical null distribution for α_g using two randomizations $E^1_{g,t}$ and $\widehat{E^2_{g,t}}$. The 99.9$^{\text{th}}$ percentile value of $P_{null}(\alpha_g)$ was 0.05, making $\alpha_g = 0.2$ a conservative threshold. Finally, we counted the number of temporally differentially expressed (tDE) genes identified in each layer (Figure S3H)

Separation of cell classes and subclasses using Seurat: In addition to clustering each time separately in SCANPY, Seurat (version 3.1, (Satija et al., 2015) was used to cluster data from all times and conditions together. This analysis was done to evaluate class and subclass level clustering, and to provide a framework to broadly check gene expression for FISH experiments in all subclasses at all times collectively. Seurat clustering was performed using two methods with similar final results. In the log-normalization based method, data were log normalized and scaled to 10,000 transcripts per cell, with 2000 variable genes used. In the generalized linear model method "SCTransform" (Hafemeister and Satija, 2019), normalization was used with 3000 variable genes. In both methods cells with fewer than 1000 or over 6000 genes or >1% mitochondrial content were filtered out. PCA was performed and unsupervised clustering was applied to the top 80 PCs. Major cell type markers from (Tasic et al., 2016) and (Tasic et al., 2018) were used to assign class and subclass designations to clusters. Clusters having two or more major markers were discarded as "doublet/debris" clusters, and clusters that were solely composed of one or two replicates were also discarded as debris clusters. In both log-normalization and SCT clustering by Seurat, the P8 cortico-cortical projecting excitatory neurons clustered separately from similar subclass neurons of later time points. Thus, P8 was clustered separately, and cell IDs from P8-only clustering were used to re-label the corresponding P8 cells in the full dataset. Class and subclass level clustering results matched SCANPY-based results (Figure S2J).

Differential gene expression analysis using Seurat: The Seurat-based clustering results were primarily used to assess subclass-level differentially expressed genes. Gene signatures of each cell subclass at different time points were identified with the FindMarkers function, performing pairwise time or condition comparisons and by comparing one time point to the average of others (a second method only used normally reared datasets). Genes were considered if they were present in 10% of cells, 0.25 log fold enriched (1.28 fold-change or more), and had a Benjamini-Hochberg corrected $P<0.05$. Of these, genes that were 0.4 log fold enriched (1.5-fold change or more) were classified as enriched.

Quantification and statistical analysis—Information for statistical analysis for all experiments and computational analyses are provided in the figure legends. Detailed descriptions of these statistical approaches can be found in the STAR Methods.

Supplementary Material

Refer to Web version on PubMed Central for supplementary material.

ACKNOWLEDGEMENTS

The authors would like to thank Maria del Carmen Diaz de la Loza for illustrations. Select images were made using BioRender. We thank Xiang Li, Michael Mashock, and Xinmin Li from UCLA Technology Center for Genomics and Bioinformatics for assistance with scRNA-seq. We also thank Andrew Elkins and Damon Polioudakis and Dan Geschwind for advice and help at early stages in this project. We thank João Couto for advice on AAV injections and Dilja Krueger-Burg for *Igsf9b* mutant mice. We are grateful to Weizhe Hong, Jonathan Flint, Emilie Marcus, Dario Ringach, and Joshua Sanes, and members of the Shekhar and Zipursky labs for critical feedback. We thank Bosiljka Tasic, Hongkui Zeng, and others at the Allen Institute for helpful discussions. This work was supported by the Stein Eye Institute EyeSTAR program (S.C.), NSF Graduate Research Fellowship (grant DGE1752814 to S.B.), an NIH grant (R00EY028625 to K.S.), a grant from the W.M. Keck Foundation to S.L.Z and J.T.T., an NIH grant

(EY023871 to J.T.T.), and startup funds from the University of California, Berkeley (K.S). S.L.Z. is an investigator of the Howard Hughes Medical Institute.

REFERENCES

Ackman JB, Burbridge TJ, and Crair MC (2012). Retinal waves coordinate patterned activity throughout the developing visual system. Nature 490, 219–225. [PubMed: 23060192]

Arneson D, Zhang G, Ying Z, Zhuang Y, Byun HR, Ahn IS, Gomez-Pinilla F, and Yang X (2018). Single cell molecular alterations reveal target cells and pathways of concussive brain injury. Nat Commun 9, 3894. [PubMed: 30254269]

Becht E, McInnes L, Healy J, Dutertre CA, Kwok IWH, Ng LG, Ginhoux F, and Newell EW (2018). Dimensionality reduction for visualizing single-cell data using UMAP. Nat Biotechnol.

Berg J, Sorensen SA, Ting JT, Miller JA, Chartrand T, Buchin A, Bakken TE, Budzillo A, Dee N, Ding SL, et al. (2021). Human neocortical expansion involves glutamatergic neuron diversification. Nature 598, 151–158. [PubMed: 34616067]

Cembrowski MS, Bachman JL, Wang L, Sugino K, Shields BC, and Spruston N (2016). Spatial Gene-Expression Gradients Underlie Prominent Heterogeneity of CA1 Pyramidal Neurons. Neuron 89, 351–368. [PubMed: 26777276]

Cembrowski MS, and Menon V (2018). Continuous Variation within Cell Types of the Nervous System. Trends Neurosci 41, 337–348. [PubMed: 29576429]

Chen T, and Guestrin C (2016). XGBoost: A Scalable Tree Boosting System. arXiv 1603.02754v3.

Espinosa JS, and Stryker MP (2012). Development and plasticity of the primary visual cortex. Neuron 75, 230–249. [PubMed: 22841309]

Franklin KP, G (2012). Paxinos and Franklin's the Mouse Brain in Stereotaxic Coordinates, Compact, 4th edn (Elsevir).

Gordon JA, and Stryker MP (1996). Experience-dependent plasticity of binocular responses in the primary visual cortex of the mouse. J Neurosci 16, 3274–3286. [PubMed: 8627365]

Gouwens NW, Sorensen SA, Berg J, Lee C, Jarsky T, Ting J, Sunkin SM, Feng D, Anastassiou CA, Barkan E, et al. (2019). Classification of electrophysiological and morphological neuron types in the mouse visual cortex. Nat Neurosci 22, 1182–1195. [PubMed: 31209381]

Hafemeister C, and Satija R (2019). Normalization and variance stabilization of single-cell RNA-seq data using regularized negative binomial regression. Genome Biol 20, 296. [PubMed: 31870423]

Haghverdi L, Buettner F, and Theis FJ (2015). Diffusion maps for high-dimensional single-cell analysis of differentiation data. Bioinformatics 31, 2989–2998. [PubMed: 26002886]

Harris KD, and Mrsic-Flogel TD (2013). Cortical connectivity and sensory coding. Nature 503, 51–58. [PubMed: 24201278]

Hensch TK (2004). Critical period regulation. Annu Rev Neurosci 27, 549–579. [PubMed: 15217343]

Hensch TK (2005). Critical period plasticity in local cortical circuits. Nat Rev Neurosci 6, 877–888. [PubMed: 16261181]

Hinojosa AJ, Deogracias R, and Rico B (2018). The Microtubule Regulator NEK7 Coordinates the Wiring of Cortical Parvalbumin Interneurons. Cell Rep 24, 1231–1242. [PubMed: 30067978]

Hooks BM, and Chen C (2020). Circuitry Underlying Experience-Dependent Plasticity in the Mouse Visual System. Neuron 107, 986–987. [PubMed: 32910891]

Hrvatin S, Hochbaum DR, Nagy MA, Cicconet M, Robertson K, Cheadle L, Zilionis R, Ratner A, Borges-Monroy R, Klein AM, et al. (2018). Single-cell analysis of experience-dependent transcriptomic states in the mouse visual cortex. Nat Neurosci 21, 120–129. [PubMed: 29230054]

Katz LC, and Shatz CJ (1996). Synaptic activity and the construction of cortical circuits. Science 274, 1133–1138. [PubMed: 8895456]

Kim EJ, Zhang Z, Huang L, Ito-Cole T, Jacobs MW, Juavinett AL, Senturk G, Hu M, Ku M, Ecker JR, et al. (2020). Extraction of Distinct Neuronal Cell Types from within a Genetically Continuous Population. Neuron 107, 274–282 e276. [PubMed: 32396852]

Kim MH, Znamenskiy P, Iacaruso MF, and Mrsic-Flogel TD (2018). Segregated Subnetworks of Intracortical Projection Neurons in Primary Visual Cortex. Neuron 100, 1313–1321 e1316. [PubMed: 30415996]

Kishi JY, Lapan SW, Beliveau BJ, West ER, Zhu A, Sasaki HM, Saka SK, Wang Y, Cepko CL, and Yin P (2019). SABER amplifies FISH: enhanced multiplexed imaging of RNA and DNA in cells and tissues. Nat Methods 16, 533–544. [PubMed: 31110282]

Ko H, Cossell L, Baragli C, Antolik J, Clopath C, Hofer SB, and Mrsic-Flogel TD (2013). The emergence of functional microcircuits in visual cortex. Nature 496, 96–100. [PubMed: 23552948]

Ko H, Mrsic-Flogel TD, and Hofer SB (2014). Emergence of feature-specific connectivity in cortical microcircuits in the absence of visual experience. J Neurosci 34, 9812–9816. [PubMed: 25031418]

Korsunsky I, Millard N, Fan J, Slowikowski K, Zhang F, Wei K, Baglaenko Y, Brenner M, Loh PR, and Raychaudhuri S (2019). Fast, sensitive and accurate integration of single-cell data with Harmony. Nat Methods 16, 1289–1296. [PubMed: 31740819]

La Chioma A, Bonhoeffer T, and Hubener M (2019). Area-Specific Mapping of Binocular Disparity across Mouse Visual Cortex. Curr Biol 29, 2954–2960 e2955. [PubMed: 31422884]

Li M, Cui Z, Niu Y, Liu B, Fan W, Yu D, and Deng J (2010). Synaptogenesis in the developing mouse visual cortex. Brain Res Bull 81, 107–113. [PubMed: 19751806]

Lu W, Bromley-Coolidge S, and Li J (2017). Regulation of GABAergic synapse development by postsynaptic membrane proteins. Brain Res Bull 129, 30–42. [PubMed: 27453545]

Lyckman AW, Horng S, Leamey CA, Tropea D, Watakabe A, Van Wart A, McCurry C, Yamamori T, and Sur M (2008). Gene expression patterns in visual cortex during the critical period: synaptic stabilization and reversal by visual deprivation. Proc Natl Acad Sci U S A 105, 9409–9414. [PubMed: 18606990]

Majdan M, and Shatz CJ (2006). Effects of visual experience on activity-dependent gene regulation in cortex. Nat Neurosci 9, 650–659. [PubMed: 16582906]

Mardinly AR, Spiegel I, Patrizi A, Centofante E, Bazinet JE, Tzeng CP, Mandel-Brehm C, Harmin DA, Adesnik H, Fagiolini M, et al. (2016). Sensory experience regulates cortical inhibition by inducing IGF1 in VIP neurons. Nature 531, 371–375. [PubMed: 26958833]

McQuin C, Goodman A, Chernyshev V, Kamentsky L, Cimini BA, Karhohs KW, Doan M, Ding L, Rafelski SM, Thirstrup D, et al. (2018). CellProfiler 3.0: Next-generation image processing for biology. PLoS Biol 16, e2005970. [PubMed: 29969450]

Meister M, Wong RO, Baylor DA, and Shatz CJ (1991). Synchronous bursts of action potentials in ganglion cells of the developing mammalian retina. Science 252, 939–943. [PubMed: 2035024]

Motta A, Berning M, Boergens KM, Staffler B, Beining M, Loomba S, Hennig P, Wissler H, and Helmstaedter M (2019). Dense connectomic reconstruction in layer 4 of the somatosensory cortex. Science 366.

Munoz-Castaneda R, Zingg B, Matho KS, Chen X, Wang Q, Foster NN, Li A, Narasimhan A, Hirokawa KE, Huo B, et al. (2021). Cellular anatomy of the mouse primary motor cortex. Nature 598, 159–166. [PubMed: 34616071]

Nakashima A, Ihara N, Shigeta M, Kiyonari H, Ikegaya Y, and Takeuchi H (2019). Structured spike series specify gene expression patterns for olfactory circuit formation. Science 365.

Network BICC (2021). A multimodal cell census and atlas of the mammalian primary motor cortex. Nature 598, 86–102. [PubMed: 34616075]

O'Leary TP, Sullivan KE, Wang L, Clements J, Lemire AL, and Cembrowski MS (2020). Extensive and spatially variable within-cell-type heterogeneity across the basolateral amygdala. Elife 9.

Ortiz C, Carlen M, and Meletis K (2021). Spatial Transcriptomics: Molecular Maps of the Mammalian Brain. Annu Rev Neurosci 44, 547–562. [PubMed: 33914592]

Peng YR, Shekhar K, Yan W, Herrmann D, Sappington A, Bryman GS, van Zyl T, Do MTH, Regev A, and Sanes JR (2019). Molecular Classification and Comparative Taxonomics of Foveal and Peripheral Cells in Primate Retina. Cell 176, 1222–1237 e1222. [PubMed: 30712875]

Reh RK, Dias BG, Nelson CA 3rd, Kaufer D, Werker JF, Kolb B, Levine JD, and Hensch TK (2020). Critical period regulation across multiple timescales. Proc Natl Acad Sci U S A 117, 23242–23251. [PubMed: 32503914]

Sanes JR, and Zipursky SL (2020). Synaptic Specificity, Recognition Molecules, and Assembly of Neural Circuits. Cell 181, 536–556. [PubMed: 32359437]

Satija R, Farrell JA, Gennert D, Schier AF, and Regev A (2015). Spatial reconstruction of single-cell gene expression data. Nat Biotechnol 33, 495–502. [PubMed: 25867923]

Scala F, Kobak D, Bernabucci M, Bernaerts Y, Cadwell CR, Castro JR, Hartmanis L, Jiang X, Laturnus S, Miranda E, et al. (2020). Phenotypic variation of transcriptomic cell types in mouse motor cortex. Nature.

Stuart T, Butler A, Hoffman P, Hafemeister C, Papalexi E, Mauck WM 3rd, Hao Y, Stoeckius M, Smibert P, and Satija R (2019). Comprehensive Integration of Single-Cell Data. Cell 177, 1888–1902 e1821. [PubMed: 31178118]

Tan L, Ringach DL, Zipursky SL, and Trachtenberg JT (2021). Vision is required for the formation of binocular neurons prior to the classical critical period. Curr Biol.

Tan L, Tring E, Ringach DL, Zipursky SL, and Trachtenberg JT (2020). Vision Changes the Cellular Composition of Binocular Circuitry during the Critical Period. Neuron 108, 735–747 e736. [PubMed: 33091339]

Tasic B, Menon V, Nguyen TN, Kim TK, Jarsky T, Yao Z, Levi B, Gray LT, Sorensen SA, Dolbeare T, et al. (2016). Adult mouse cortical cell taxonomy revealed by single cell transcriptomics. Nat Neurosci 19, 335–346. [PubMed: 26727548]

Tasic B, Yao Z, Graybuck LT, Smith KA, Nguyen TN, Bertagnolli D, Goldy J, Garren E, Economo MN, Viswanathan S, et al. (2018). Shared and distinct transcriptomic cell types across neocortical areas. Nature 563, 72–78. [PubMed: 30382198]

Traag VA, Waltman L, and van Eck NJ (2019). From Louvain to Leiden: guaranteeing well-connected communities. Sci Rep 9, 5233. [PubMed: 30914743]

Tropea D, Kreiman G, Lyckman A, Mukherjee S, Yu H, Horng S, and Sur M (2006). Gene expression changes and molecular pathways mediating activity-dependent plasticity in visual cortex. Nat Neurosci 9, 660–668. [PubMed: 16633343]

Wang BS, Sarnaik R, and Cang J (2010). Critical period plasticity matches binocular orientation preference in the visual cortex. Neuron 65, 246–256. [PubMed: 20152130]

Wiesel TN, and Hubel DH (1963). Single-Cell Responses in Striate Cortex of Kittens Deprived of Vision in One Eye. J Neurophysiol 26, 1003–1017. [PubMed: 14084161]

Wojtowicz WM, Vielmetter J, Fernandes RA, Siepe DH, Eastman CL, Chisholm GB, Cox S, Klock H, Anderson PW, Rue SM, et al. (2020). A Human IgSF Cell-Surface Interactome Reveals a Complex Network of Protein-Protein Interactions. Cell 182, 1027–1043 e1017. [PubMed: 32822567]

Wolf FA, Angerer P, and Theis FJ (2018). SCANPY: large-scale single-cell gene expression data analysis. Genome Biol 19, 15. [PubMed: 29409532]

Wolf FA, Hamey FK, Plass M, Solana J, Dahlin JS, Gottgens B, Rajewsky N, Simon L, and Theis FJ (2019). PAGA: graph abstraction reconciles clustering with trajectory inference through a topology preserving map of single cells. Genome Biol 20, 59. [PubMed: 30890159]

Wolock SL, Lopez R, and Klein AM (2019). Scrublet: Computational Identification of Cell Doublets in Single-Cell Transcriptomic Data. Cell Syst 8, 281–291 e289. [PubMed: 30954476]

Woo J, Kwon SK, Nam J, Choi S, Takahashi H, Krueger D, Park J, Lee Y, Bae JY, Lee D, et al. (2013). The adhesion protein IgSF9b is coupled to neuroligin 2 via S-SCAM to promote inhibitory synapse development. J Cell Biol 201, 929–944. [PubMed: 23751499]

Xu HP, Furman M, Mineur YS, Chen H, King SL, Zenisek D, Zhou ZJ, Butts DA, Tian N, Picciotto MR, et al. (2011). An instructive role for patterned spontaneous retinal activity in mouse visual map development. Neuron 70, 1115–1127. [PubMed: 21689598]

Yao Z, Liu H, Xie F, Fischer S, Adkins RS, Aldridge AI, Ament SA, Bartlett A, Behrens MM, Van den Berge K, et al. (2021a). A transcriptomic and epigenomic cell atlas of the mouse primary motor cortex. Nature 598, 103–110. [PubMed: 34616066]

Yao Z, Liu H, Xie F, Fischer S, Booeshaghi AS, Adkins RS, Aldridge AI, Ament SA, Pinto-Duarte A, Bartlett A, et al. (2020). An integrated transcriptomic and epigenomic atlas of mouse primary motor cortex cell types. BioRxiv.

Yao Z, van Velthoven CTJ, Nguyen TN, Goldy J, Sedeno-Cortes AE, Baftizadeh F, Bertagnolli D, Casper T, Chiang M, Crichton K, et al. (2021b). A taxonomy of transcriptomic cell types across the isocortex and hippocampal formation. Cell.

Yuste R, Hawrylycz M, Aalling N, Aguilar-Valles A, Arendt D, Armananzas R, Ascoli GA, Bielza C, Bokharaie V, Bergmann TB, et al. (2020). A community-based transcriptomics classification and nomenclature of neocortical cell types. Nat Neurosci 23, 1456–1468. [PubMed: 32839617]

Zeng H, and Sanes JR (2017). Neuronal cell-type classification: challenges, opportunities and the path forward. Nat Rev Neurosci 18, 530–546. [PubMed: 28775344]

Zhang M, Eichhorn SW, Zingg B, Yao Z, Cotter K, Zeng H, Dong H, and Zhuang X (2021). Spatially resolved cell atlas of the mouse primary motor cortex by MERFISH. Nature 598, 137–143. [PubMed: 34616063]

Zhu Y, Qiao W, Liu K, Zhong H, and Yao H (2015). Control of response reliability by parvalbumin-expressing interneurons in visual cortex. Nat Commun 6, 6802. [PubMed: 25869033]

Highlights

- Three glutamatergic L2/3 cell types are specified after eye opening
- L2/3 cell types are spatially segregated by graded transcriptomic distinctions
- Vision is required for the graded expression of L2/3 cell type markers
- Binocular function in L2/3 requires *Igsf9b*, a graded vision-dependent gene

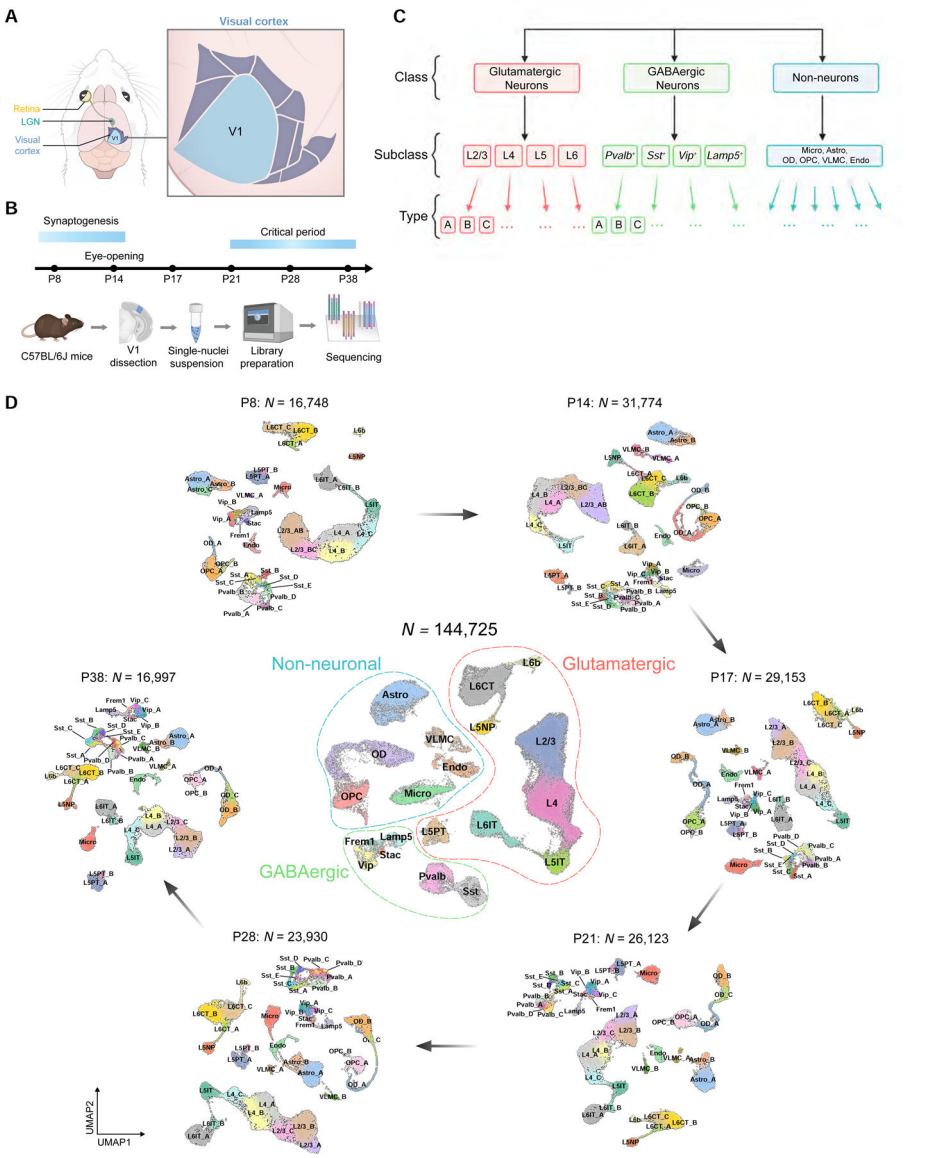

Figure 1. snRNA-seq profiling of V1 during postnatal development

A. Schematic of the mouse visual system. Primary visual cortex (V1). Surrounding higher visual areas: A, anterior; AL, anterolateral; AM, anteromedial; LI, lateralintermediate; LM, lateromedial; P, posterior; PM, posteromedial; POR, postrhinal; RL, rostrolateral; TEA, temporal anterior areas.

B. Experimental workflow of snRNA-seq profiling of V1 at six postnatal ages.

C. Cellular taxonomy of V1.

D. UMAP visualization of V1 transcriptomic diversity during postnatal development. Dots correspond to cells and distances between them reflect degrees of transcriptomic similarity. Central panel shows cells from all six ages colored by subclass identity (Table S1). Peripheral panels show cells from different ages, colored by type identity determined via clustering. Data from each age and class were analyzed separately and then merged for visualization purposes.

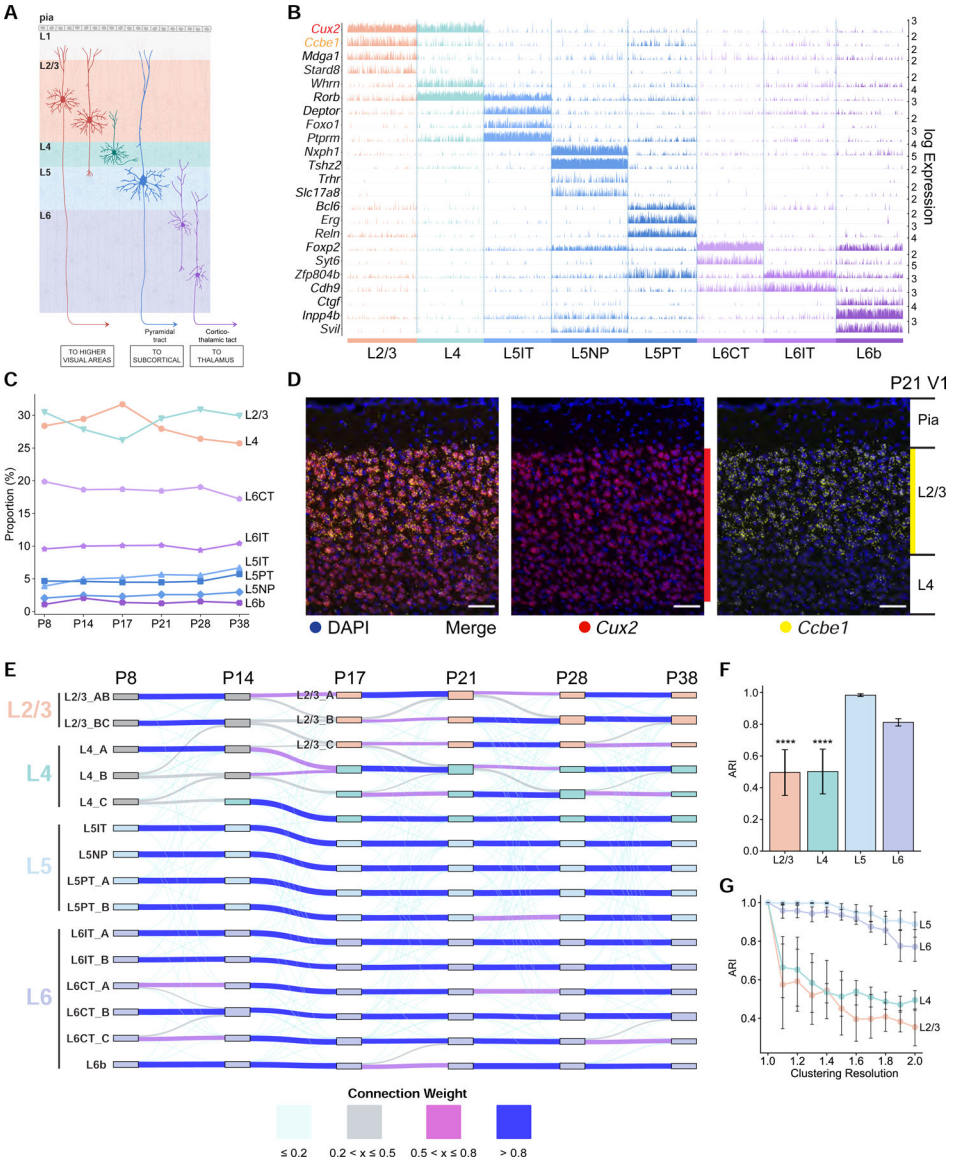

Figure 2. Transcriptomic diversity of V1 glutamatergic neurons during postnatal development

A. Schematic of glutamatergic neurons in V1 arranged in layers L1-L6.

B. Tracks plot showing subclass-specific markers (rows) in glutamatergic neurons (columns), grouped by subclass (e.g., L2/3). 1000 randomly selected cells from each subclass were used for plotting. Scale on the y-axis (right), normalized, log-transformed transcript counts in each cell. *Ccbe1*, a L2/3 marker, and *Cux2*, a L2/3/4 marker, are highlighted.

C. The proportions of glutamatergic subclasses are stable with age despite significant variation in the number of cells profiled (Table S2).

D. Coronal section through V1 analyzed by fluorescent *in situ* hybridization (FISH) at P21. *Ccbe1* is selective for L2/3 glutamatergic neurons. *Cux2* is expressed in L2/3 and L4 glutamatergic neurons and in inhibitory neurons and non-neuronal cells (see Figure S2B for other ages). Scale, 50 μm.

E. Transcriptomic similarity identifies temporal associations among V1 glutamatergic neuron types across ages. Sankey diagram computed using a supervised classification approach. Nodes, individual V1 glutamatergic neuron types at each age (as in Figure 1D); edges, colored based on transcriptomic correspondence.

F. Adjusted Rand Index (ARI) values quantifying temporal correspondence of glutamatergic types between each pair of consecutive ages based on transcriptomic similarity. Individual bars denote layers. ARI ranges from 0 (no correspondence) to 1 (perfect correspondence). Bar heights, mean ARI computed across pairs of consecutive ages; error bars, standard deviation; ***, $P<0.0001$ (one-way ANOVA) for L2/3 and L4 against L5 and L6.

G. Types in L2/3 and L4, but not L5 and L6, are sensitive to changes in clustering resolution. Glutamatergic neurons at each age are re-clustered at different values of the resolution parameter (x-axis), and the results are compared with the base case corresponding to resolution = 1 (STAR Methods). Line plots, mean ARI values for each layer (colors); error bars, standard deviation across ages.

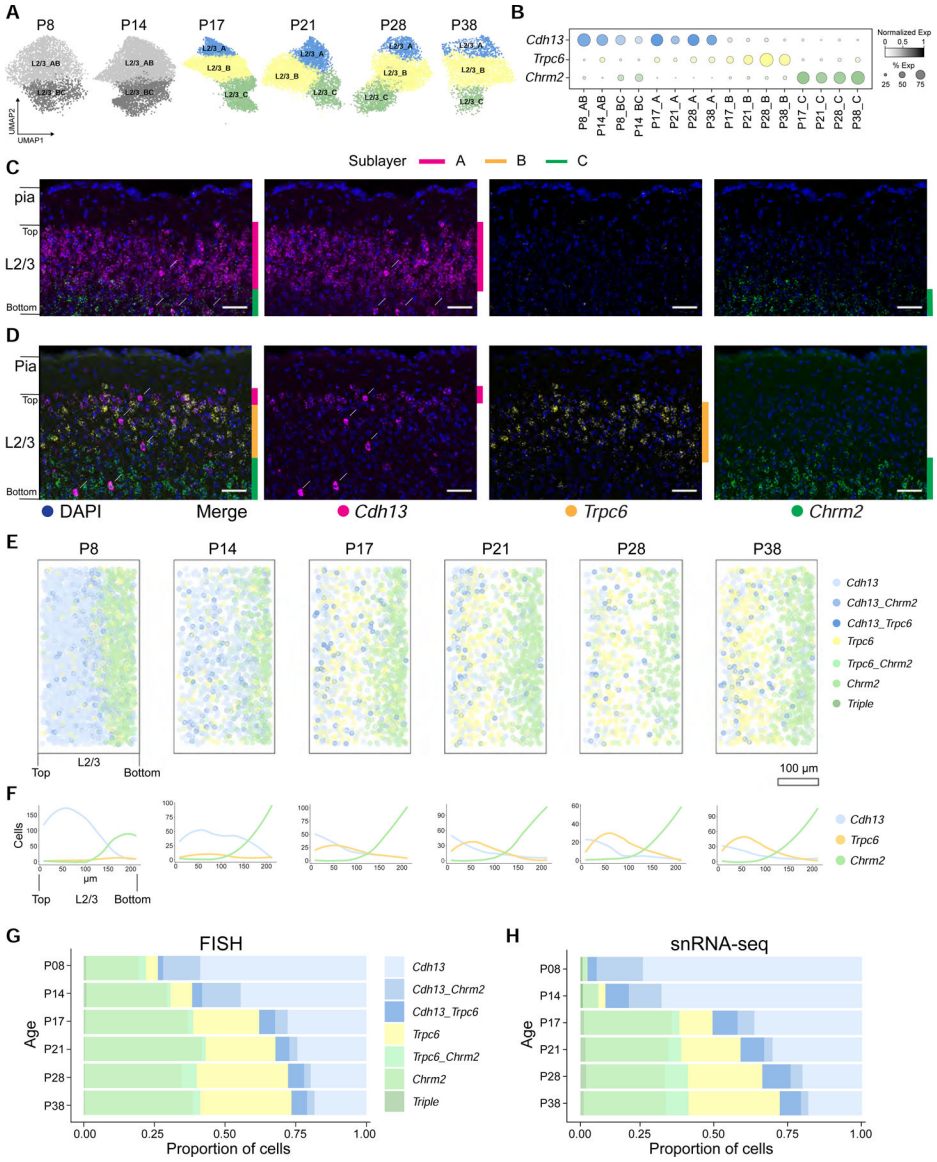

Figure 3. Anatomical and transcriptomic maturation of L2/3 glutamatergic neuron types

A. UMAP plots of L2/3 glutamatergic neuron types across ages.

B. Dot plot showing expression patterns of L2/3 type-specific genes (rows and colors) across L2/3 neuron types arranged by age (columns).

C. FISH images showing type markers *Cdh13, Trpc6,* and *Chrm2* within L2/3 at P8. Vertical colored bars, sublayers expressing the indicated markers; arrows, large cells expressing *Cdh13* are not excitatory neurons; they are a subset of inhibitory and non-neuronal cells. Scale, 50 µm.

D. Same as C, at P38.

E. Pseudo-colored representation of *Cdh13, Trpc6,* and *Chrm2* expression in L2/3 cells at six ages. Cells are colored based on expression levels of one or more of these markers. Each panel is an overlay of five or six images of V1 from three mice. Pial to ventricular axis is oriented horizontally from left to right within each panel. Total number of cells analyzed:

P8, 2324; P14, 1142; P17, 1036; P21, 1038; P28, 653; and P38, 1034. Scale bar, 100 μm. Panels E and F are rotated relative to Panels C and D. “Top” and “Bottom” are indicated.

F. Line tracings quantifying the number of cells per bin at each position along the pial to ventricular axis corresponding to panel E. 0 on the x-axis, region of L2/3 closest to pia. 14 bins were used over the depth of L2/3.

G. Relative proportions of cells within each expression group defined in panel E quantified using FISH data.

H. Same as G using snRNA-seq data.

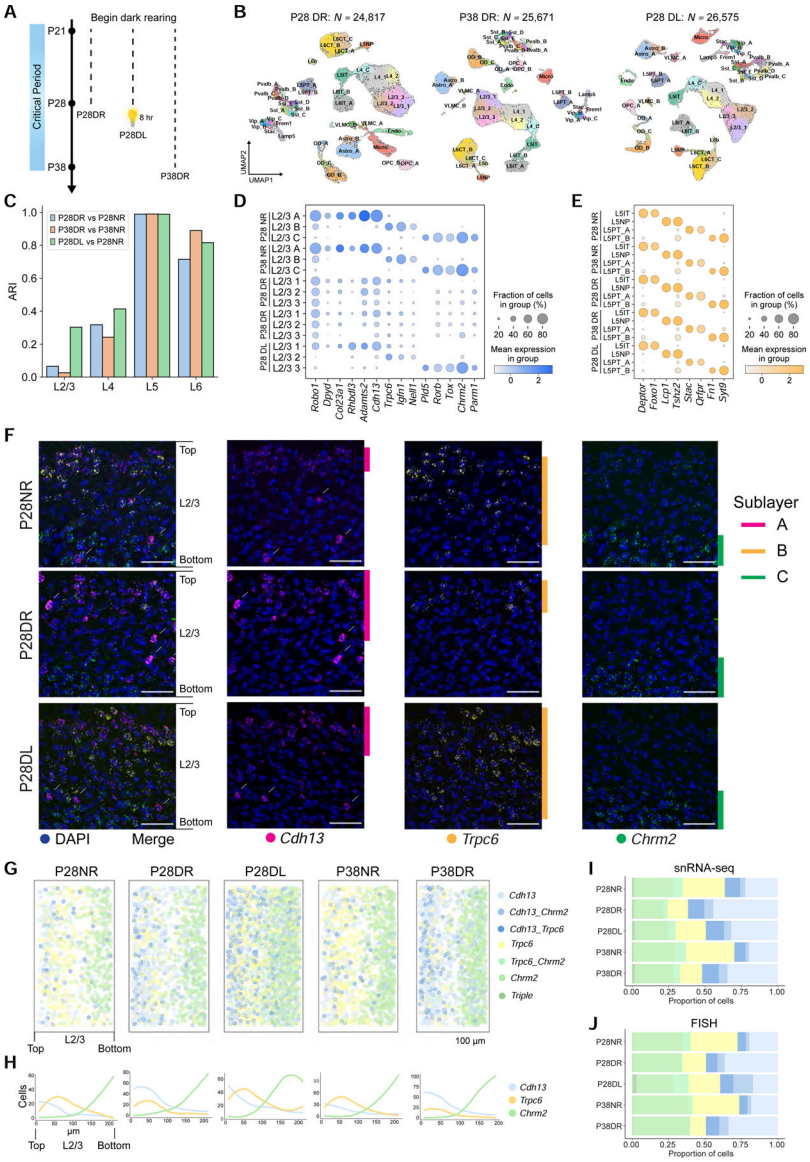

Figure 4. Visual experience is required to maintain L2/3 glutamatergic neuron types

A. Schematic of experiments. Data collected from three rearing conditions: Dark-reared between P21-P28 (P28DR) and P21-P38 (P38DR), and dark-reared between P21-P28 followed by 8 hrs (P28DL).

B. UMAP plots of transcriptomic diversity in P28DR, P38DR, and P28DL. Clusters that match 1:1 to normally-reared (NR) types in Figure 1D are labeled. This was not possible for all L2/3 and two L4 clusters, which correspond poorly to NR types. We therefore provisionally labeled these clusters L2/3_1, L2/3_2, L2/3_3, L4_1, and L4_2.

C. Adjusted Rand Index (ARI) quantifying transcriptomic similarity within each layer (x-axis) between glutamatergic clusters observed in dark-reared mice and types observed in normally-reared (NR) mice. Colors correspond to comparisons as indicated.

D. Expression of L2/3 type markers (columns) in NR, DR, and DL types and clusters (rows) at P28 and P38.

E. Same as panel D for L5. DR and DL clusters are labeled based on their tight transcriptomic correspondence with NR types (Figure S5F, G).

F. FISH images showing expression of L2/3 markers in NR, DR, and DL at P28. Arrows, inhibitory neurons expressing *Cdh13*. The level of *Cdh13* is modestly repressed by vision. Scale, 50 μm.

G. Pseudo-colored representation of *Cdh13, Trpc6,* and *Chrm2* expression in NR, DR, and DL mice at P28 and P38. Each plot is an overlay of 5–6 images of V1 from three mice. Pial to ventricular axis is oriented horizontally from left to right within each panel. Total number of cells analyzed: P28NR, 653; P28DR, 989; P28DL, 1732; P38NR, 1034; and P38DR, 1177).

H. Cells per bin at each position along the pial to ventricular axis corresponding to panel G. 0 on the x-axis, region of L2/3 closest to pia. 14 bins were used over the depth of L2/3.

I. Proportions of L2/3 cells within each expression group defined in panel G quantified using snRNA-seq data

J. Same as I using FISH data.

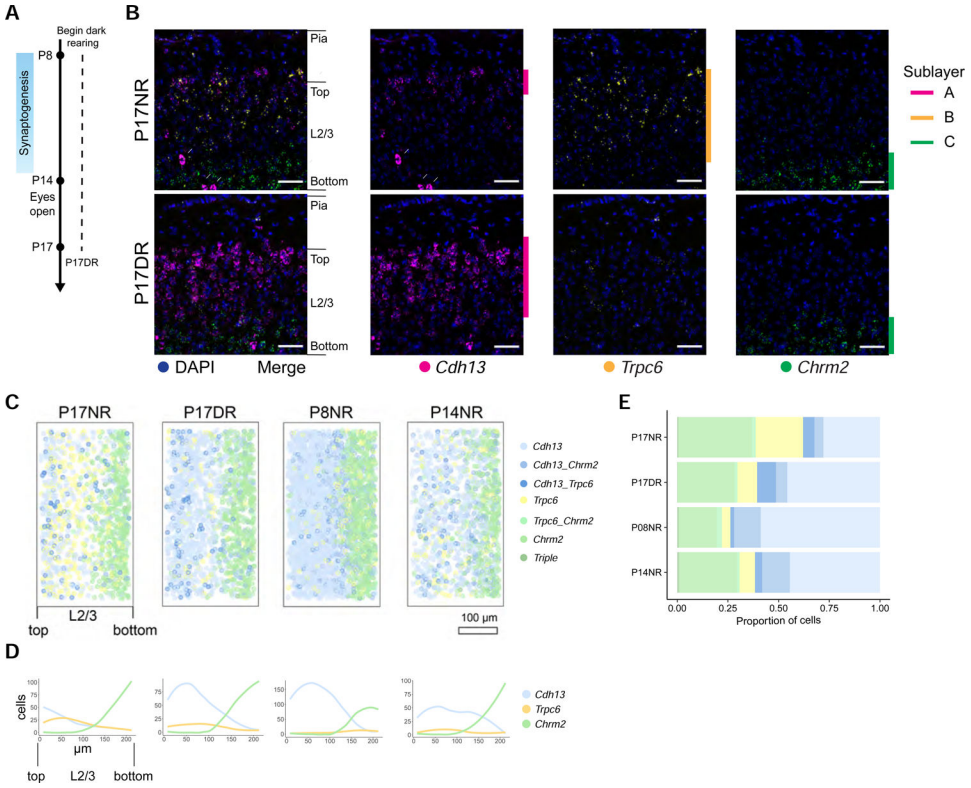

Figure 5. Vision is required to establish L2/3 glutamatergic neuron types

A. Schematic of experiments.

B. FISH images of L2/3 markers in normally-reared (NR) and dark reared (DR) mice at P17. Arrows, inhibitory neurons expressing *Cdh13*. Scale, 50 µm.

C. Pseudo-colored representation of *Cdh13, Trpc6,* and *Chrm2* expression in L2/3 cells. Each plot is an overlay of 6 images of V1 from three mice. Cells quantified: P17NR, 1036; P17DR, 1411.

D. Line tracings quantifying cells per bin at each position along the pial to ventricular axis corresponding to panel C. 0 on the x-axis, L2/3 region closest to pia. 14 bins were used over the depth of L2/3.

E. Proportions of cells in each expression group defined in panel C quantified using FISH data.

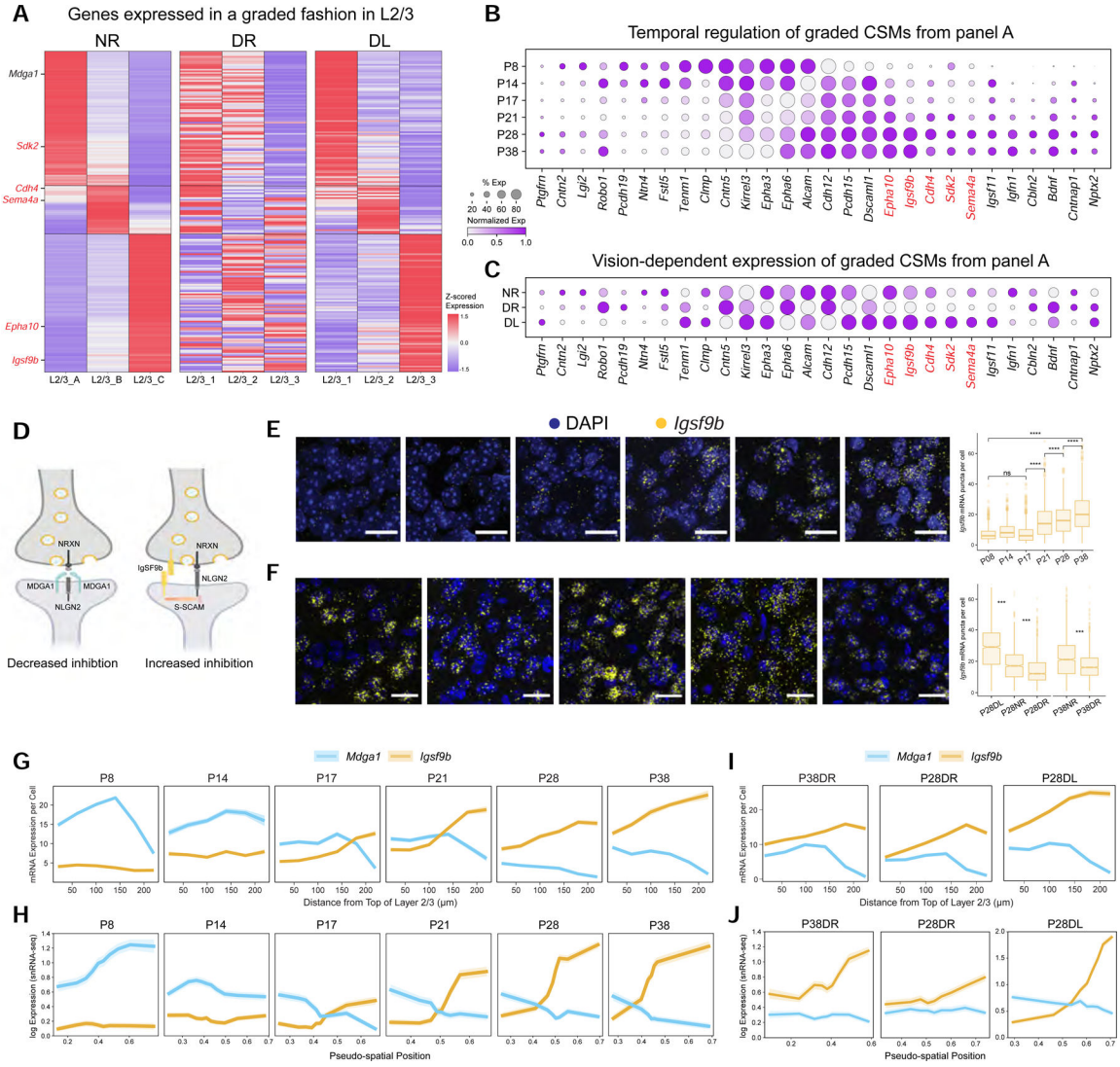

Figure 6. Continuous variation of L2/3 neuron types and vision-dependent gene gradients implicated in wiring

A. Heatmap of L2/3 type-specific genes with graded expression in normally-reared mice (NR). This is disrupted in dark-reared mice (DR) and partially recovered by exposing DR mice to light for 8 hrs (DL). For the full set of L2/3 type-specific genes grouped by expression pattern, see Figure S6A. Genes satisfying criteria in panels B and C (see text) are indicated in red lettering. Two of the three L4 cell types also exhibit graded expression differences (see Figure S6L–M).

B. Temporal regulation of cell surface molecules (CSMs) in panel A. Red print, genes upregulated during the classical critical period (P21-P38), downregulated in DR, and upregulated in DL.

C. Same illustration as panel B across the conditions P28NR, P28DR, and P28DL.

D. Schematic of MDGA1 and IGSF9B interactions with NLGN2 at synapses. MDGA1 prevents NLGN2 interaction with NRXN presynaptically. IGSF9B binds homophilically and interacts with S-SCAM postsynaptically as does NLGN2.

E. FISH images of *Igsf9b* mRNA over time in V1. Three animals per time point, six images per animal. Scale, 20 μm. (*Right*) Box plot quantifying expression. Wilcoxon Rank Sum Test, ***** P* <0.0001. Cells quantified: P8,1191; P14,1011; P17, 1389; P21, 1729; P28, 1277; and P38, 1588.

F. FISH images showing that dark rearing decreases *Igsf9b* expression in L2/3, and eight hours of light restores expression. Scale, 50 μm. (*Right*) Box plot quantifying expression. Three animals imaged per age and condition combination. Cells quantified: P28NR, 1290 cells; P28DL, 1506 cells; P28DR, 1521 cells; P38NR, 1629 cells; and P38DR, 1885. Quantified at 40X. Wilcoxon Rank Sum Test, **** P* <0.001.

G. FISH quantification of average *Mdga1* and *Igsf9b* expression (y-axis) in glutamatergic cells as a function of distance from the top of L2/3 (x-axis). Shaded ribbons represent standard error of the mean. Cells quantified: P8, 2204; P14, 928; P17, 1037; P21, 1183; P28, 719; and P38, 942. Data from three or four animals at each age.

H. Reconstruction of *Mdga1* and *Igsf9b* expression levels averaged across cells based on their inferred L2/3 pseudo-spatial locations in gene expression space (see STAR Methods). Shaded ribbons, standard deviation.

I. Same as panel G for P38DR, P28DR, and P28DL. Cell numbers: P38DR, 719; P28DR, 1061; and P28DL, 1053 cells. Data collected from three animals at each time point

J. Same as panel H for P38DR, P28DR, and P28DL. Note difference in scale for P28DL to capture the extent of increase in *Igfs9b* expression.

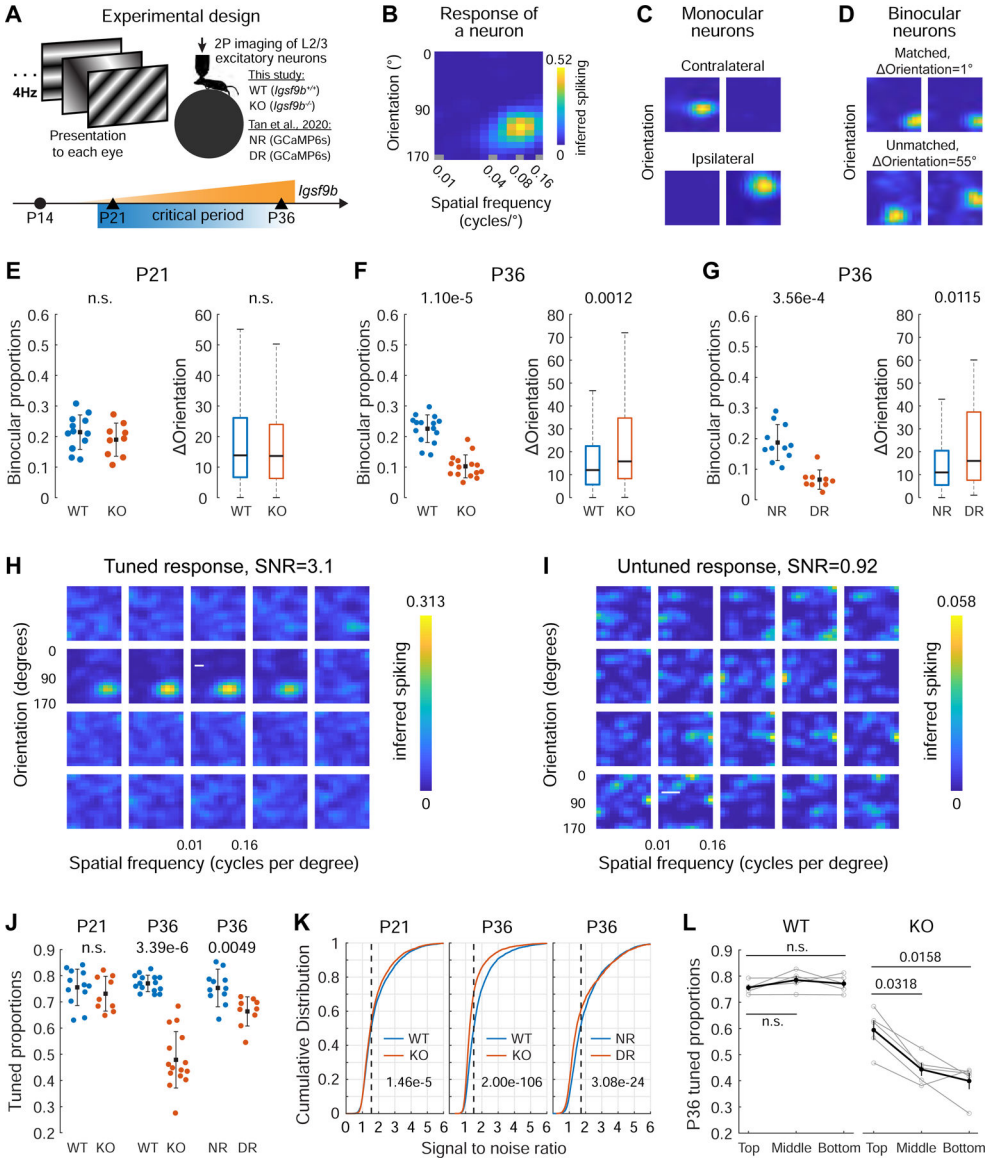

Figure 7. Igsf9B is required for vision-dependent maturation of binocular neurons in V1B L2/3

A. Experimental setup for functional analysis. (*Top*) Schematic of 2-photon (2P) Ca^{2+} imaging using different sinusoidal gratings sequentially presented at 4 Hz. Visual stimuli were presented to each eye separately. The head-fixed mouse was awake on a running wheel. Mice used in this study are WT (*Igsf9B*$^{+/+}$) and KO (*Igsf9B*$^{-/-}$) expressing AAV encoded jGCaMP7f. Panels G, J, K include our unpublished results from NR and DR (dark reared from P22-P36) transgenic mice carrying GCaMP6s expressed in excitatory neurons (from Tan et al., 2020). (*Bottom*) WT and KO mice were imaged at P21 and P36, the onset and closure of the classical critical period, respectively. Orange, *Igsf9*b *m*RNA levels in L2/3 as a function of time.

B. Tuning kernel showing response of a single neuron (see Figure S7L) to the contralateral eye. The colors represent response strength (color bar, right) as a function of stimulus orientations (Y-axis) and spatial frequency (log scale; X-axis).

C. Response to contralateral (C) and ipsilateral eye (I) of monocular cells. Kernels for each neuron were normalized to the peak inferred spiking.

D. As in C, but for matched (*top*) and unmatched (*bottom*) binocular neurons. ΔOrientation, the difference in orientation preference between the two eyes.

E. (*Left*) proportions of binocular neurons in WT and KO mice at P21. Each point is from a single imaging plane. Mean and standard deviation, black dots and lines. Mann-Whitney U test. (*Right*) ΔOrientation of binocular neurons in WT (4 mice, 761 cells) and KO (3 mice, 619 cells) mice at P21. Black horizontal line, median; box, quartiles with whiskers extending to 2.698σ. Mann-Whitney U test. Note the absence of phenotype in binocular neurons at P21.

F. As in E but for binocular neurons at P36. WT, 5 mice, 602 cells; KO, 5 mice, 269 cells.

G. As in F but for binocular neurons in NR (4 mice, 339 cells) and DR (3 mice, 78 cells) mice. P36 phenotypes in KO and DR mice were similar. The difference in proportion between the WT (panel F) and NR (panel G) likely reflects differences in genetic background or experimental design (i.e., viral versus transgenic expression of GCaMP or differences between GCaMP6s and jGCaMP7f).

H. Example of a tuned cell from a WT mouse at P21. Inferred spiking as a function of imaging frames for a neuron with a tuned response. Numbers at the top left indicate imaging frames relative to stimulus onset. For this neuron, the SNR is 3.1, and peak response occurred 5 imaging frames or 323 ms after onset of its optimal stimuli, consistent with the kinetics of jGCaMP7f.

I. As in H but for an untuned cell in the same mouse at P21.

J. Proportions of tuned neurons in WT and KO mice at P21 and P36, and in NR and DR mice at P36. Each point is from a single imaging plane. Mean and standard deviation, black dots and lines. Mann-Whitney U test.

K. (*Left*) Cumulative distribution of SNR to either eye of all imaged neurons at P21 in WT (4 mice, 3436 neurons) or KO (3 mice, 3457 neurons) mice. Dashed vertical line marks the SNR threshold for visually evoked responses (see STAR Methods). *P*-value from two-sample Kolmogorov-Smirnov test is shown in the plot. (*Middle*) As in the left, but for mice at P36 in WT (5 mice, 2698 neurons) and KO (5 mice, 2699 neurons). (*Right*) As in the middle, but for neurons in NR (4 mice, 1905 neurons) and DR (3 mice, 1188 neurons) mice. Neuronal responses to each eye were measured separately.

L. Proportions of tuned neurons as a function of depth in V1B L2/3 in WT and KO mice at P36. Top, middle, and bottom indicate the three imaging planes covering the corresponding sub-laminae within L2/3 in each mouse. Each gray line represents a mouse. Mean and standard error of the mean were shown as black dots and vertical lines. Mann-Whitney U test with Bonferroni correction.